Core cross-linked polymeric micelles based on polypept(o)ides: from secondary structure formation of polypeptides to functional cross-linking strategies for polymeric micelles

Bauer, T.A.

8

Core Cross-Linked Polymeric Micelles for Specific Iron Delivery: Inducing Sterile Inflammation in Macrophages

SPION-Loaded Core Cross-Linked Polymeric Micelles Induce Sterile Inflammation
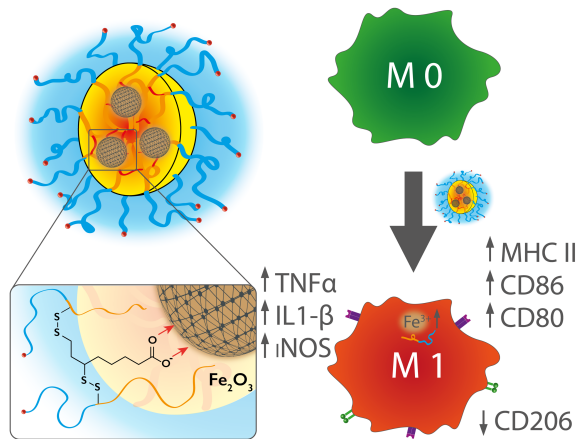
Core Cross-Linked Polymeric Micelles for Specific Iron Delivery: Inducing Sterile Inflammation in Macrophages

Tobias A. Bauer[‡,a,b], Natalie K. Horvat[‡,c,d,e], Oriana Marques[d,f], Sara Chocarro[g], Christina Mertens[f], Silvia Colucci[d,f], Sascha Schmitt[h], Luca M. Carrella[b], Svenja Morsbach[h], Kaloian Koynov[h], Federico Fenaroli[i], Peter Blümler[j], Michaela Jung[k], Rocio Sotillo[g,e], Matthias W. Hentze[*,c], Martina U. Muckenthaler[*,d,e,f], Matthias Barz[*,a,b]

[‡] These authors contributed equally to this work.

[a] Leiden Academic Centre for Drug Research (LACDR), Leiden University, Einsteinweg 55, 2333CC Leiden, The Netherlands

[b] Department of Chemistry, Johannes Gutenberg University Mainz, Duesbergweg 10-14, 55128 Mainz, Germany

[c] European Molecular Biology Laboratory (EMBL), [◊]Collaboration for joint PhD degree between EMBL and the Faculty of Biosciences, University of Heidelberg, Meyerhofstr.1, 69117 Heidelberg, Germany.

[d] Molecular Medicine Partnership Unit (MMPU), Otto-Meyerhof-Zentrum, Im Neuenheimer Feld 350, 69120 Heidelberg, Germany.

[e] Translational Lung Research Center Heidelberg (TLRC), German Center for Lung Research (DZL), University of Heidelberg, Im Neuenheimer Feld 350, 69120 Heidelberg, Germany.

[f] Department of Pediatric Oncology, Hematology, Immunology, and Pulmonology, Heidelberg University Hospital, Im Neuenheimer Feld 350, 69120 Heidelberg, Germany.

[g] Department of Molecular Thoracic Oncology, German Cancer Research Center (DKFZ), Im Neuenheimer Feld 280, 69120 Heidelberg, Germany.

[h] Max Planck Institute for Polymer Research, Ackermannweg 10, 55128 Mainz, Germany.

[i] Department for Biosciences, University of Oslo, Blindernveien 31, 0371 Oslo, Norway.

[j] Institute of Physics, Johannes Gutenberg University Mainz, Staudingerweg 9, 55128 Mainz, Germany.

k Institute of Biochemistry I, Faculty of Medicine, Goethe-University Frankfurt, Theodor-Stern-Kai 7, 60590 Frankfurt am Main, Germany.

Abstract

Iron is an essential co-factor for cellular processes. In the immune system, it can activate macrophages and represents a potential therapeutic for various diseases. To specifically deliver iron to macrophages, iron oxide nanoparticles were embedded in polymeric micelles of reactive polysarcosine-*block*-poly(*S*-ethylsulfonyl-L-cysteine). Upon surface functionalization *via* dihydrolipoic acid, iron oxide cores act as crosslinker themselves and undergo chemoselective disulfide bond formation with the surrounding poly(*S*-ethylsulfonyl-L-cysteine) block, yielding glutathione-responsive core cross-linked polymeric micelles (CCPMs). When applied to primary murine and human macrophages, these nanoparticles displayed preferential uptake, sustained intracellular iron release, and induced a strong inflammatory response. This response was also demonstrated *in vivo* when nanoparticles were intratracheally administered to wild-type C57Bl/6N mice. Most importantly, the controlled release concept to deliver iron oxide in redox-responsive CCPMs induces significantly stronger macrophage activation than any other iron source at identical iron levels (e.g., Feraheme), directing to a new class of immune therapeutics.

Keywords

macrophage polarization · iron metabolism · polypept(o)ide · polymeric micelle · cross-linking · immunomodulation

Cover page

Designed to release: Core Cross-linked micelles based on polypept(o)ides have been designed for specific delivery of iron to macrophages and trigger sterile inflammation. Iron recognition leads to feedback mechanisms for preferred cell uptake, inducing macrophage activation. The approach abolishes undesired immune tolerance unleashing the potential of iron as therapeutic agent.

Introduction

Diseases, such as cancer, atherosclerosis, traumatic nerve injury, and autoimmune disorders are hallmarked by inflammation, whereby infiltration of innate immune cells can exacerbate the disease condition.[1–5] Phagocytic cells, such as monocytes and monocyte-derived macrophages comprise a significant proportion of these infiltrating cells, and a growing number of macrophage subtypes were identified, which are characterized by different functional capabilities, depending on niche-derived stimuli, such as cytokines, chemokines, and metabolites.[6–10] Recruited monocyte-derived macrophages residing in the periphery of solid tumors can mediate adaptive immunity, promote angiogenesis, tissue remodeling and repair, and often contribute to the aggressiveness of a cancer's invasive front.[11–13] Apart from immune functions, macrophages play a pivotal role in maintaining iron homeostasis, as they recycle hemoglobin-derived iron from senescent red blood cells.[14–17] The intricate connection between the immune function of macrophages and their role in iron metabolism was demonstrated by the exposure to metabolites, such as free heme or iron, that directly affect the macrophage activation state, leading to not only changes in the expression of iron-regulatory genes but also in innate immune effector functions.[1,18] By locally applying iron in the form of superparamagnetic iron oxide nanoparticles (SPIONs) within the tumor microenvironment (TME), macrophages become activated, a process that can correlate with inhibition of tumor growth.[1,19] In previous studies, Ferumoxytol (Feraheme, Rienso), a formulation of an iron oxide nanoparticle in a matrix of covalently cross-linked carbohydrates (polyglucose sorbitol carboxymethylether), was used as iron source.[19–23] Despite its approval for the treatment of iron deficiency anemia in patients with chronic kidney disease, the original intention of Ferumoxytol was as a contrast agent for magnetic resonance imaging designed for minimal iron release.[24–30] We now propose that delivery systems which allow for controlled iron release in the TME can serve as immunotherapeutic agent.

SPION-loaded core cross-linked polymeric micelles (SPION-CCPMs) were developed based on polysarcosine-*block*-poly(*S*-ethylsulfonyl-L-cysteine) copolypept(o)ides.[31,32] In these systems, cross-linking by chemoselective disulfide formation features glutathione (GSH)-dependent particle degradation inside the endo- or phagosomal pathway of macrophages.[33]

Results and Discussion

The polymer synthesis was performed by nucleophilic ring-opening polymerization of a-amino acid *N*-carboxyanhydrides (NCAs), yielding polypept(o)ides of polysarcosine-*block*-poly(*S*-ethylsulfonyl-L-cysteine) (pSar-*b*-pCys(SO$_2$Et)).[31,32,34] As shown in Figure 1, block copolymers were obtained using a bifunctional initiator approach, leading to polymers P1 - P3 with chain lengths of 170 to 225 for polysarcosine and 17 to 31 for poly(*S*-ethylsulfonyl-L-cysteine), well suited for steric shielding and cross-linking.[35,36] The syntheses were accomplished on a gram-scale, yielding 2.9 g of P2 and 2.3 g of P3 (Scheme S1, Table S1, and Figure S1 - S5) demonstrating the scalability of the presented approach. For nanoparticle preparation, oleic acid-coated SPIONs (γ-maghemite, Fe$_2$O$_3$, D = 6 nm) were solubilized with the amphiphilic pSar-*b*-pCys(SO$_2$Et) block copolymers, cross-linked with dihydrolipoic acid, and labeled on the amine end-group with Cy5-NHS ester (Figure 1). During co-self-assembly, initial solvent mixtures of chloroform and dimethyl sulfoxide (DMSO) were exchanged stepwise to pure DMSO and water, resulting in SPION-CCPMs as an aqueous dispersion. In addition to disulfide bond formation, dihydrolipoic acid enables direct grafting onto the iron oxide nanoparticle surface by substituting oleic acid, connecting the respective building blocks and stabilizing SPION encapsulation (Figure 1D). Unconjugated dye, residual oleic acid, and free polymer were removed by extraction and repetitive ultra-filtration (MWCO 100 kDa) yielding SPION-CCPM^{Cy5} as a dark green aqueous dispersion (Figure 1E, S9).

To serve as control nanoparticles, empty core cross-linked polymeric micelles (CCPMs) were prepared from pSar-*b*-pCys(SO$_2$Et), according to previous reports (Table S2, Figure S6 and S7).[35,37]

The illustration of SPION-CCPMs as spherical structures containing multiple SPION cores was derived from nanoparticle characterization, which is summarized in Figure 1 and Table 1. According to single-angle dynamic light scattering (DLS), co-self-assembly of oleic acid-coated SPIONs and P3 (mass ratio 1:1) yielded micelles with a hydrodynamic diameter (D_h) of 71 nm (Figure 1A), whereby the size slightly increased to D_h = 82 nm upon cross-linking, dye conjugation, and particle purification. Importantly, the narrow size distribution (PDI ≤ 0.16) of SPION-CCPMs^{Cy5} remained identical when particles were lyophilized and re-constituted in water (SPION-CCPM^{Cy5}-Lyo), which facilitates their scalability and pharmaceutical use.[38]
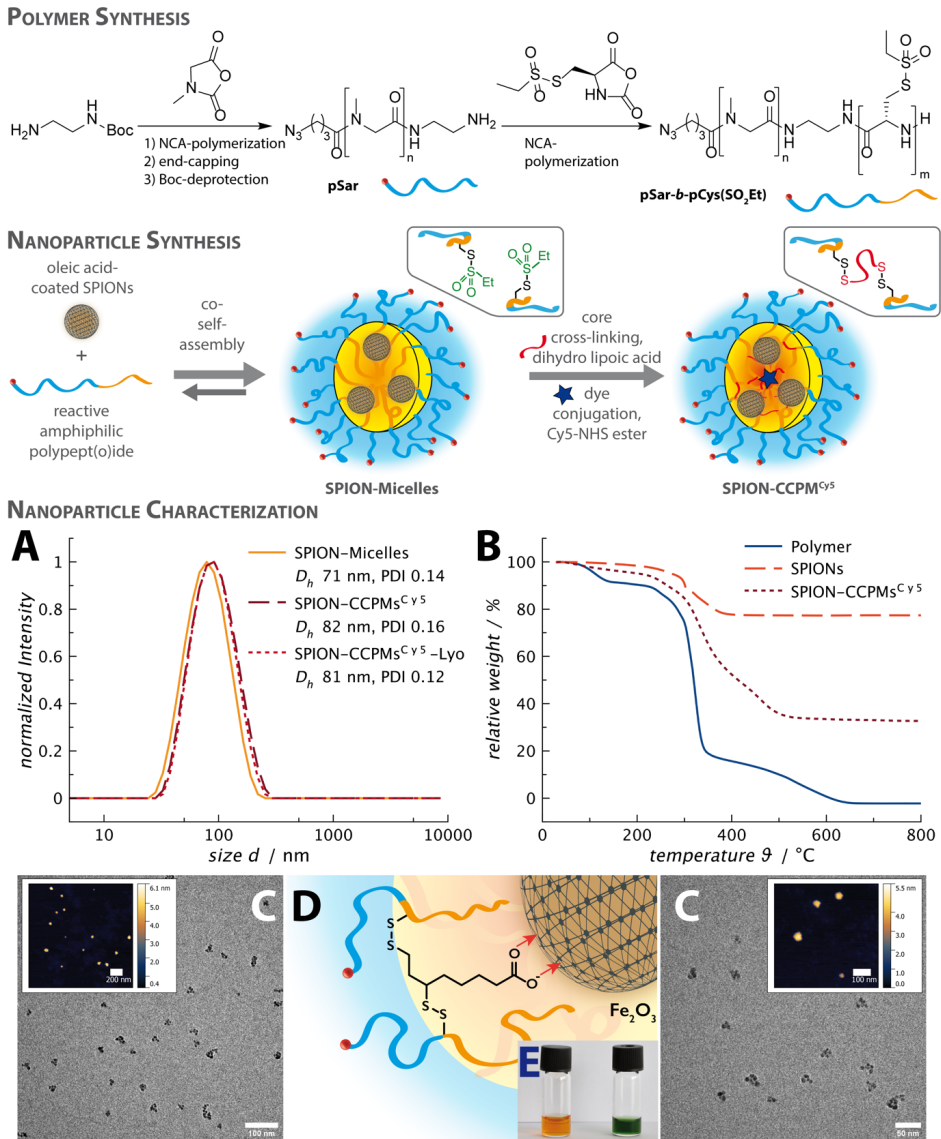
POLYMER SYNTHESIS

NANOPARTICLE SYNTHESIS

NANOPARTICLE CHARACTERIZATION

Figure 1. Polymer and nanoparticle synthesis, and characterization of SPION-CCPMs. (**A**) Single-angle DLS of SPION-Micelles and SPION-CCPM^{Cy5} before and after lyophilization and redispersion in water (lyo). (**B**) Iron oxide quantification by TGA in pure O_2 atmosphere. (**C**) Analysis of SPION-CCPM^{Cy5} by AFM and TEM. (**D**) Illustrated surface grafting by the carboxyl group of the lipoic acid cross-linker in the micellar core. (**E**) Image of SPION-CCPM dispersions in MilliQ water before (left) and after dye-labeling (right).

Table 1. Analytical results of the polymer synthesis.

particle	polymer[a]	wt% Fe_2O_3[b] / %	D_h[c] / nm	D_h[d] / nm	ξ-potential[c] / mV
SPION-CCPM[Cy5]	P3, pSar$_{170}$-*b*-pCys(SO$_2$Et)$_{27}$	33.0	-	37.7	45.7
CCPM[Cy5]	P1, pSar$_{225}$-*b*-pCys(SO$_2$Et)$_{31}$	-	44	39.2	54.0

[a] pSar chain lengths relative to pSar standards, pCys(SO$_2$Et) chain lengths derived from ^{1}H NMR, [b] TGA in pure O_2 atmosphere, [c] single-angle DLS at a scattering angle of 173°, [d] fluorescence correlation spectroscopy.

Morphological analysis of SPION-CCPMs by atomic force microscopy (AFM) revealed spherical structures with sizes below 100 nm (Figure 1C), congruent with DLS and fluorescence correlation spectroscopy (FCS) (Table 1, Figure S10). Transmission electron microscopy (TEM) was used to elucidate the encapsulated SPION cores. SPIONs were organized in patterns of local clusters with total dimensions below 50 nm containing multiple cores each (Figure 1C, S11). The individual SPION cores showed diameters of 6 to 10 nm. In contrast, oleic acid-coated SPIONs were randomly arranged (Figure S12). Since the polymer shell could not be visualized due to large contrast discrepancies, the observed local clustering emphasizes successful encapsulation of iron oxide nanoparticles into core cross-linked polymeric micelles.[39–41] Taken together, AFM and TEM analysis affirm the structure of SPION-CCPMs as spherical nano-sized containers with multiple iron oxide nanoparticles embedded. The quantification of iron in lyophilized SPION-CCPMs was performed by thermogravimetric analysis (TGA) in a pure O_2 atmosphere. At these conditions, the polymeric matrix is entirely oxidized, and the remnant corresponds to iron oxide (Fe_2O_3) (Figure 1B).[42] For SPION-CCPMs, an iron oxide content of 33 weight% was determined (Table 1). Moreover, SPION-CCPMs were analyzed by Fourier transform infrared (FT-IR) spectroscopy. Characteristic peaks at 2853, 1738, and 1709 cm^{-1} corresponding to oleic acid dissipated upon encapsulation, and peaks of the polymer backbone (3470 cm^{-1}, 3275 cm^{-1} (amide N-H), 1633 cm^{-1} (amide C=O)) were detected (Figure S8), indicating complete replacement of the oleic acid-coating and successful surface functionalization by lipoic acid.[43]

The superparamagnetic nature of SPION-CCPMs was confirmed by magnetization hysteresis loops recorded at temperatures of 300 K and 5 K. No significant remanence magnetization could be detected and a blocking

temperature of 42 K was obtained corresponding to iron oxide nanoparticles with a diameter of approximately 10 nm (Figure S13).[44] Accordingly, the SPION-CCPM^{Cy5} dispersion showed response to magnetic fields (Figure S14) without aggregation. In an *in vitro* setting, particles could be guided by a combined dipolar/quadrupolar magnetic field (supplementary video).[45,46] However, no signs of magnetic guidance were distinguishable in zebrafish larvae (see SI for further details).
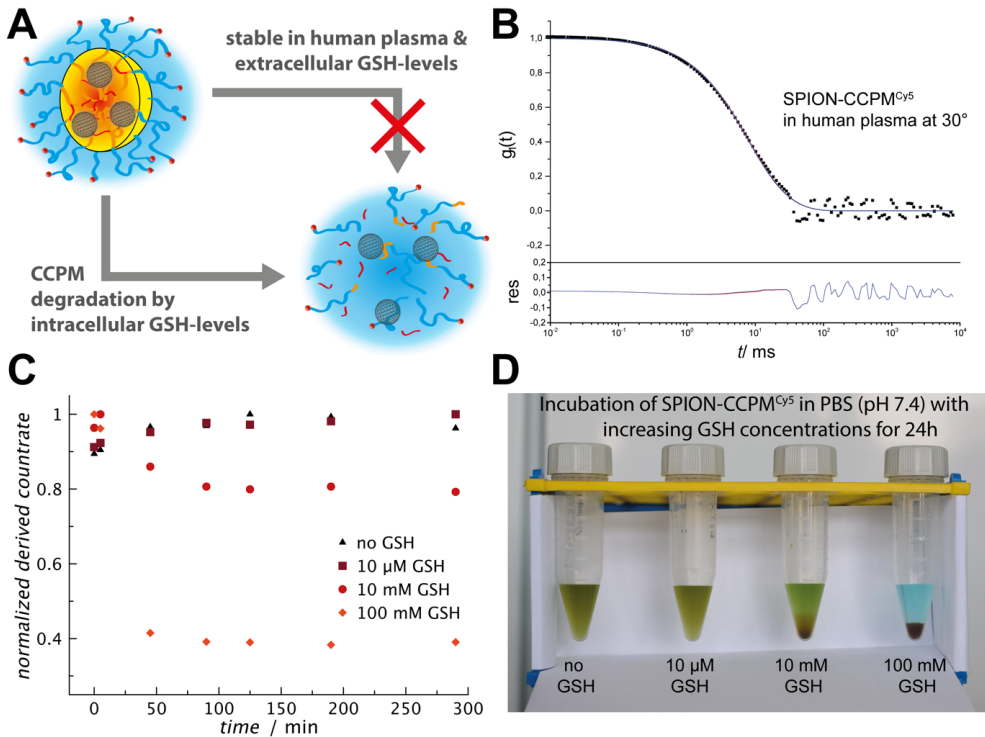

Figure 2. SPION-CCPMs display colloidal stability and stimuli-responsive degradation. (**A**) Concept of intracellular iron release inside macrophages (**B**) Multi-angle DLS of SPION-CCPM^{Cy5} in undiluted human plasma: autocorrelation function g$_1$(t) for an exemplary scattering angle of 30° together with fits with (blue line) and without (red line) additional aggregate term (upper graph), and the corresponding residuals between fit w/o aggregate and correlation function. (**C**) Glutathione (GSH)- induced particle degradation after incubation in carbonate buffer (pH 7.4) at 37 °C detected by single-angle DLS. (**D**) GSH-induced degradation performed in phosphate buffer (pH 7.4, 37 °C) after 24 h.

To account for colloidal stability, SPION-CCPMs were analyzed by multi-angle DLS in human blood plasma, following the procedure by Rausch *et al.*[47] Here, no aggregation was detected after incubation of SPION-CCPM[Cy5] in human blood plasma at a nanoparticle concentration of 0.1 g ·L^{-1} (Figure 2B). Moreover, SPION-CCPM[Cy5] remained intact even during analysis by gel permeation chromatography (GPC) in hexafluoroisopropanol (Figure S8), a good solvent for pSar-*b*-pCys(SO$_2$Et) copolymers. The absence of unconjugated dye was further verified by FCS (Figure S10).[48] SPION-CCPMs[Cy5] exhibit a slightly negative ζ-potential of -5.1 mV, comparable to empty CCPMs, accounting for efficient compensation of the iron oxide surface charge by lipoic acid as well as sufficient shielding by the polysarcosine corona (Figure S8).[49] The stimuli-responsive behavior of disulfide cross-linked SPION-CCPMs was evaluated by DLS in carbonate buffer (pH 7.4) at GSH concentrations present in the endo-phagosomal compartments of macrophages.[50] At extracellular GSH levels (10 µM) the derived count rate remains constant, while a decrease was observed at intracellular GSH levels (10 mM) indicating particle degradation (Figure 2C).[35] Interestingly, when conducted in phosphate buffer (pH 7.4), precipitation of iron oxide/phosphate is observed for SPION-CCPMs treated with GSH concentrations above 10 µM (Figure 2D), exemplifying the combination of stability in blood-like conditions with triggered (redox-dependent) release of the encapsulated iron.

When tested in cell lines or primary murine and human cells, the internalization of nanoparticles was measured by intracellular fluorescent intensity using fluorescence-activated cell sorting (FACS) and fluorescence microscopy. In a co-culture of Lewis lung carcinoma cells (LLCs) and primary murine bone marrow-derived macrophages (BMDMs), SPION-CCPMs appear to sequester mainly in macrophages. *Vice versa,* LLCs accumulate more CCPMs than SPION-CCPMs (Figure 3A), suggesting that iron released from SPION-CCPMs may further reduce SPION-CCPM uptake in LLCs, in a negative feedback manner. The iron released from SPION-CCPMs likely stimulates BMDMs' uptake rate. This leads to a remarkable ~100-fold difference in relative nanoparticle uptake between the epithelial and myeloid cell type. These results indicate that SPION-CCPMs are preferably taken up by macrophages and not by other cell types (primary hepatocytes, LLCs; Figure S17). To further explore whether SPION-CCPMs release iron inside macrophages and if it is metabolically active, we analyzed the expression of iron regulatory genes in BMDMs. After 1 hour incubation, SPION-CCPMs was detected in BMDMs (Figure S18) but iron was not detected to the

same extent as BMDMs treated with a dose-matched iron source ferric ammonium citrate (FAC) (Figure 3B). After 24 hours, BMDMs treated SPION-CCPMs show iron accumulation to a similar extent as FAC treated BMDMs (Figure 3B), indicating a sustained release profile.

At the molecular level, iron accumulation decreased *transferrin receptor 1* mRNA (Tfrc) and protein expression (TFR1) (Figure 3C) also seen in BMDMs treated with FAC (20 µM) or lipopolysaccharide (LPS), which can trigger iron sequestration in pro-inflammatory macrophages.[7,11,15]

Iron accumulation in cells triggers oxidative stress and target gene expression of the oxidative stress responsive transcription factor nuclear factor E2-related factor-2(Nrf2)/BTB and CNC homolog 1 basic leucine zipper (bZIP) transcription factor 1 (Bach1) signaling pathway.[51] Expression of two Nrf2 target genes, *HO-1* (Figure 3C) and *Fpn1* (Figure 3D), are strongly induced in macrophages treated with SPION-CCPMs. At an early time point (4 hours), ROS levels induced by SPION-CCPM treatment were high in the cytoplasm and low in nuclear and mitochondrial regions (Figure 3E), suggesting that iron is released into the cytoplasm soon after nanoparticle internalization. Of note, 18 hours after SPION-CCPM treatment, ROS detection shifted to nuclear and mitochondrial compartments (Figure 3F), similar to FAC treated cells. Importantly, CCPMs did not increase ROS levels in BMDMs, suggesting that iron released from the SPION-CCPMs specifically triggers ROS production. Taken together, these data support the concept of SPION-CCPMs, which degrade slowly so that BMDMs safely handle internalized particles without detectable cellular toxicity (Figure S19). Most importantly, the released iron is metabolically active and able to alter iron metabolism and oxidative defense.
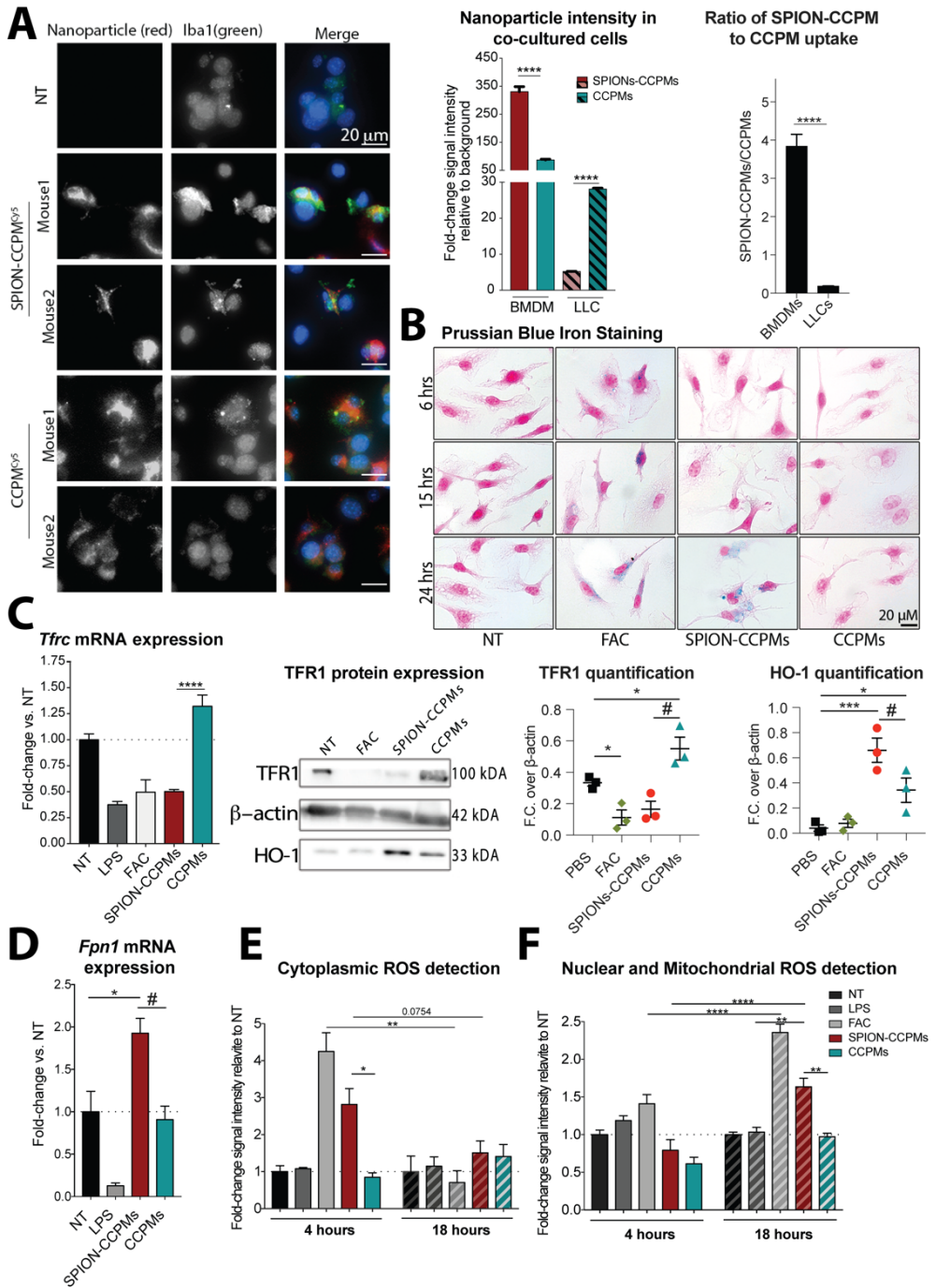
A

Nanoparticle (red) Iba1(green) Merge

NT

SPION-CCPM^{cy5} — Mouse1 / Mouse2

CCPM^{cy5} — Mouse1 / Mouse2

20 μm

Nanoparticle intensity in co-cultured cells

Fold-change signal intensity relative to background

**** ****

SPIONs-CCPMs
CCPMs

BMDM LLC

Ratio of SPION-CCPM to CCPM uptake

SPION-CCPMs/CCPMs

****

BMDMs LLCs

B

Prussian Blue Iron Staining

6 hrs

15 hrs

24 hrs

NT FAC SPION-CCPMs CCPMs

20 μM

C

Tfrc mRNA expression

Fold-change vs. NT

****

NT LPS FAC SPION-CCPMs CCPMs

TFR1 protein expression

NT FAC SPION-CCPMs CCPMs

TFR1 — 100 kDA
β–actin — 42 kDA
HO-1 — 33 kDA

TFR1 quantification

F.C. over β-actin

* #
*

PBS FAC SPIONs-CCPMs CCPMs

HO-1 quantification

F.C. over β-actin

* #
***

PBS FAC SPIONs-CCPMs CCPMs

D

Fpn1 mRNA expression

Fold-change vs. NT

* #

NT LPS SPION-CCPMs CCPMs

E

Cytoplasmic ROS detection

Fold-change signal intensity relavite to NT

0.0754
**
*

4 hours 18 hours

F

Nuclear and Mitochondrial ROS detection

Fold-change signal intensity relavite to NT

NT
LPS
FAC
SPION-CCPMs
CCPMs

**** ****
**
**

4 hours 18 hours

Figure 3. *In vitro* analysis of SPION-CCPMs. (**A**) Co-culture of LLCs and BMDMs incubated with SPION-CCPMs[Cy5] and CCPMs[Cy5] or not treated (NT). Representative fluorescence microscopy images and Cy5 fluorescence detection by FACS after 24 hours. (**B**) Detection of released iron by Perls' Prussian blue staining. Cells were counterstained with nuclear fast red (pink). (**C**) Detection of transferrin receptor (*Tfrc*) mRNA as well as TFR1 and heme oxygenase 1 (HO-1) protein by qPCR and western blot. mRNA expression was corrected to *Rpl19* expression. (**D**) Ferroportin (*Fpn1*) mRNA expression after 6 hours. (**E**) Cytoplasmic or nuclear and (**F**) mitochondrial ROS detection using CELLROX Orange and CELLROX Green probes in BMDMs after 4- and 18-hours. Fluorescent intensities produced by ROS probes were measured by FACS and represented as fold-change compared to non-treated (NT) condition. Data reported as n ± Standard Error of the Mean (SEM) and representative of 3 independent experiments. One-way ANOVA(*) or students t-test(#): * $p < 0.01$, ** $p < 0.001$, *** $p < 0.0001$.

The exposure of macrophages to heme or non-transferrin bound iron has been reported to activate an inflammatory state, hallmarked by increased expression of inflammatory cytokines, such as interleukin (IL)-1a/b, IL-6, and tumor necrosis factor (TNF)a, as well as elevated surface proteins, such as Cluster of Differentiation (CD) 86, CD80, and Class II major histocompatibility complex molecules (MHC II).[1,19,52] We analyzed these important markers of inflammation in BMDMs exposed to LPS or IL4, serving as positive and negative controls, respectively, and 20 μM of FAC, SPION-CCPMs, as well as the non-loaded CCPMs. BMDMs treated with SPION-CCPMs remarkably increase the expression of MHC II, CD80, CD301 and CD86, similar to LPS stimulated cells (Figure 4A). Similarly, inflammatory cytokines and enzymes, such as *Tnfa, Il6, Il1b, Nos2,* and *Cxcl10* were significantly upregulated (Figure 4B). In contrast, expression of the mannose receptor, CD206, an indicator of anti-inflammatory activation, was reduced in BMDMs exposed to SPION-CCPMs compared to those with CCPMs (Figure 4A). Notably, the specific inflammatory response to SPION-CCPMs was also reflected in human macrophages (Figure 4D, Figure S20).
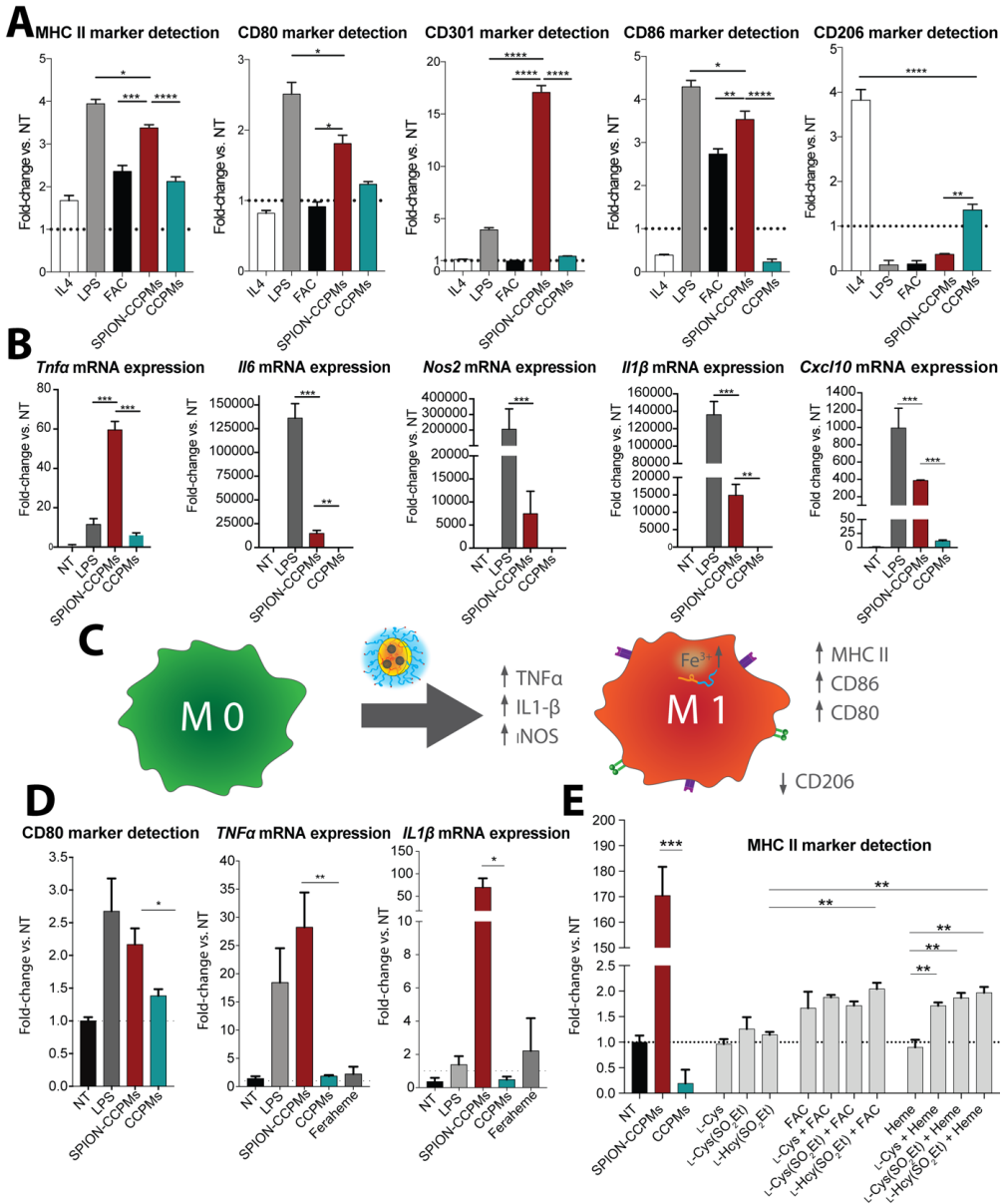
Figure 4. SPION-CCPMs induce sterile inflammation in macrophages. (**A**) Cell surface protein expression and (**B**) mRNA expression levels of inflammatory cytokines and chemokines in primary murine BMDM after 24 or 6 hours, respectively. (**C**) Illustration of the inflammatory response. (**D**) Upregulation of inflammatory mRNA and protein expression in human macrophages. (**E**) Cell surface marker MHC II expression for

individual CCPM components. (**A-E**) All graphs represent data as fold change compared to the non-treated condition (NT) and mRNA expression were corrected to *Rpl19*. Data reported as n ± SEM and representative of 3 independent experiments. One-way ANOVA: * $p < 0.05$, ** $p < 0.01$, *** $p < 0.001$, **** $p < 0.0001$.

Iron delivery by SPION-CCPMs induces a remarkably robust pro-inflammatory response in human and murine macrophages (Figure 4), an effect that is significantly more pronounced than for feraheme (ferumoxytol) at identical iron levels. To understand the basis of this effect, we tested individual components of the polypept(o)ide-based delivery system, such as L-cysteine, *S*-ethylsulfonyl-L-cysteine (L-Cys(SO$_2$Et)) or analogous *S*-ethylsulfonyl-L-homocysteine (L-Hcy(SO$_2$Et), either alone or in combination with heme and FAC. When added with iron, L-Cys(SO$_2$Et) and L-Hcy(SO$_2$Et) induced expression of MHC II and CD86, albeit to a much lower extent than intact SPION-CCPMs (Figure 4E and S21). We thus propose that the chemical nature of the nanoparticles together with the intracellular iron release are responsible for the observed strong inflammatory responses. Examination of the gene expression changes (Figure 4) indicate sterile inflammation is triggered by SPION-CCPMs, resembling LPS-like inflammation in macrophages. Differences were observed for mRNA expression of arginase-1, Nrf2 target genes, NAD(P)H dehydrogenase (quinone) 1, and Glutathione *S*-Transferase Mu 1 (Figure S22). We thus speculate that SPION-CCPM treatment induces a combination of signaling pathways through both iron and inflammatory patterns.[22]

To verify that SPION-CCPMs can also induce inflammation *in vivo*, the nanoparticles were applied to wild-type C57Bl/6N mice (Figure 5A). Female mice, aged 6-8 weeks, were intratracheally instilled with PBS or SPION-CCPMs. At 4 h and 24 h post-treatment, mice were sacrificed and evaluated for immune cell recruitment and iron content in the lungs. Among other indications, we expect the developed SPION-CCPMs to be highly beneficial for the application as an adjuvant in cancer therapy.[1,53] Since the lungs are densely populated with macrophages and offer the advantage to apply SPION-CCPMs non-invasively to macrophages reducing off-target immune activation in other organs, intratracheal administration is a preferable application route.[12,54–57]
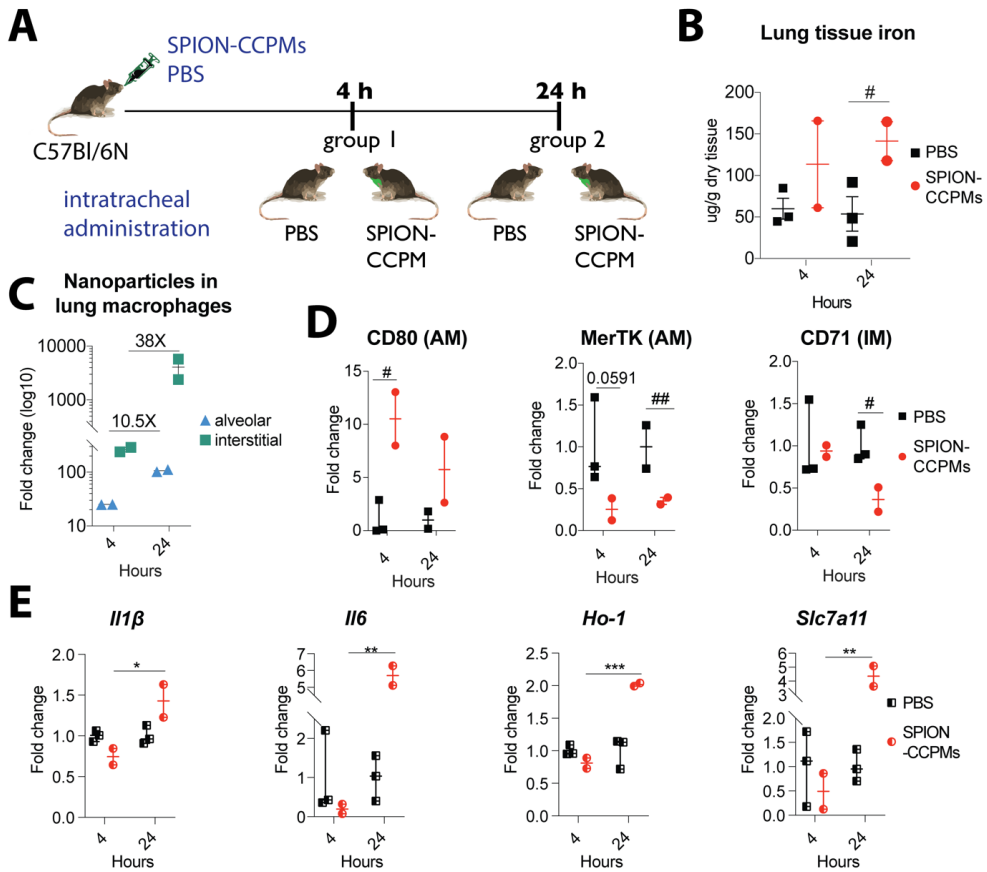
Figure 5. SPION-CCPMs induce inflammation in vivo. (**A**) C57Bl/6 mice were analyzed 4 h and 24 h after intratracheal administration of SPION-CCPMs or PBS as control. (**B**) non-heme iron levels in lung tissue. (**C**) Nanoparticle uptake in interstitial (IM) and alveolar (AM) macrophages. (**D**) Cell surface protein expression on AM and IM. (**E**) Analysis of mRNA expression of inflammatory cytokines and enzymes in total lung tissue. One-way ANOVA(*) or students' t-test (#): * $p < 0.05$, ** $p < 0.01$, *** $p < 0.001$, **** $p < 0.0001$.

We found that at 24 h after instillation, non-heme iron content increased ~3-fold in the lungs of SPION-CCPMs administered mice compared to PBS administered mice (Figure 5B). Furthermore, FACS analysis demonstrated that SPION-CCPMs could be detected in both, alveolar (AM) and interstitial (IM) macrophages as early as 4 h following application. The intensity of SPION-CCPMs increased significantly in both cell types at the 24 h time point (Figure 5C), indicating that

IM and AM are rapidly taking up SPION-CCPMs. We speculate that the difference in uptake between these two populations may be explained by their residing location within the lungs. The intratracheal instillation applied here delivers SPION-CCPMs to the bronchus of the lungs where IMs are mainly localized. This may explain the brighter SPION signal in IMs 4h after SPION-CCPMs application compared to AM that are located in the alveolar space and thus take longer time to reach.[58,59] We next evaluated the inflammatory response in the lungs of mice upon administration of either PBS or SPION-CCPMs. Cell surface marker expression in AM and IM were quantified by FACS, and mRNA expression of pro-inflammatory cytokines and enzymes were analyzed in total lung tissue. At both time points analyzed, AM showed increased expression of CD80 (a known inflammatory protein) and lacked expression of C-Mer proto-oncogene tyrosine kinase (MerTK, a protein expressed under conditions when inflammation resolves), demonstrating macrophage inflammatory activation by SPION-CCPM administration.[13,60] IM were also responsive to SPION-CCPMs, showing reduced CD71 levels at the 24 h time point indicating a time-dependent intracellular degradation of SPION-CCPMs triggering a well-known response to iron accumulation (Figure 5D). This observation parallels our findings of SPION-CCPM treatment of BMDMs in cell culture (Figure 3B,C). The inflammatory response in lung tissue was further substantiated by showing time-dependent expression of the pro-inflammatory cytokines *Il1b* and *Il6*, as well as of oxidative stress response enzymes *Ho-1* and *Slc7a11* (Figure 5E). Notably, the delayed inflammatory response program at the 24 h time point substantiates findings in cultured cells (Figure 4) that suggest that SPION-CCPMs induce inflammation distinctly from LPS.[61] Taken together, we show that SPION-CCPMs induce sterile activation of macrophages in cell-based assays and in the mouse lung, illustrating the significant potential for the activation of macrophages as an adjuvant therapy.

Conclusion

Our study demonstrates that specific delivery of an iron source to macrophages can trigger pronounced pro-inflammatory responses, both *in vitro* (primary murine and human cells) and *in vivo* (C57Bl/6N mouse model). The design concept of polypept(o)ide-based SPION-CCPMs combines steric shielding and surface functionalization of SPIONs featuring colloidal stability and stimuli-responsive degradation, whereby the iron becomes available to macrophages upon internalization within 24 hours by cleavage of the disulfide cross-links in the nanoparticle core. In primary murine and human macrophages, the sustained release of iron induces sterile inflammation as indicated by pro-inflammatory surface marker expression and cytokine secretion, resembling a shift towards an M1-like phenotype. This effect was confirmed *in vivo* following intratracheal administration of SPION-CCPMs to wild-type C57Bl/6N mice. Due to the immunomodulatory properties, SPION-CCPMs outcompete established iron oxide nanoparticles like Feraheme, making them a promising adjuvant therapy for the treatment of diseases, such as in autoimmune disorders, traumatic nerve injury, or interventions of the tumor microenvironment of solid cancers.

Experimental Section

Materials and Instrumentation: Unless stated otherwise, solvents were purchased from Sigma Aldrich. THF and n-hexane were dried over Na and freshly distilled prior to use. DMF was bought from Acros (99.8 %, Extra Dry over Molecular Sieve), freshly freeze-pumped prior to use to remove residual dimethyl amine, and handled in the absence of light. HFIP was purchased from Fluorochem, deuterated solvents from Deutero and were used as received. MilliQ water was prepared using a MILLI-Q® Reference A+ System. Water was used at a resistivity of 18.2 MΩ·cm^{-1} and total organic carbon of <5 ppm. Diphosgene was purchased from Alfa Aesar. Sarcosine was bought from Sigma Aldrich and dried in vacuum before NCA synthesis. N-tert-butoxycarbonyl (Boc)-1,2-diaminoethane and N,N-diisopropyl ethylamine (DIPEA) were purchased from Sigma Aldrich, fractionally distilled and stored at -78°C and -20°C, respectively. Oleic acid coated iron oxide nanoparticles were obtained from Sanofi-Aventis Deutschland GmbH, as well as obtained from Ocean Nanotech. D,L-Lipoic and was bought from TCI Europe. Pentafluorophenyl trifluoroacetate, tris(2-carboxyethyl)phosphine (TCEP·HCl) and acetic acid anhydride were obtained from Sigma Aldrich and used without further purification. Cyanine 5 NHS Ester was obtained from Lumiprobe GmbH.

Human blood plasma for DLS measurements was collected at the Transfusion Center of the University Clinic of Mainz (Germany) from ten healthy donors after physical examination and after obtaining informed consent in accordance with the Declaration of Helsinki. The study was approved by the local ethics committee "Landesärztekammer Rheinland-Pfalz" (837.439.12 (8540-F)). All plasma batches were pooled and stored at -20 °C.

Nuclear Magnetic Resonance: ^{1}H, ^{19}F and ^{13}C NMR spectra were recorded on a Bruker Avance II 400 at room temperature at a frequency of 400, 376 and 101 MHz and on a Bruker Avance III HD 300 at room temperature at a frequency of 300, 282 and 75 MHz. DOSY spectra were recorded on a Bruker Avance III HD 400 (400 MHz). Calibration of the spectra was achieved using the solvent signals. NMR spectra were analyzed with MestReNova version 12.0.4 from Mestrelab Research S.L. Degrees of polymerization (X_n) were calculated by comparing the integral of the initiator peak and the integrals of the protons for pSar and pCys(SO_2Et).

Infrared and UV-Vis Spectroscopy: Attenuated total reflectance Fourier transform infrared (ATR-FT-IR) spectroscopy was performed on a FT/IR-4100 (Jasco) with an ATR sampling accessory (MIRacle, Pike Technologies). IR spectra were analyzed using Spectra Manager 2.0 (Jasco) for integration. NCA polymerization was monitored by FT-IR spectroscopy. UV-Vis spectra were recorded using a Jasco V-630 spectrophotometer (1 cm × 1 cm quartz cell).

Gel Permeation Chromatography: Analytical GPC was performed using HFIP as eluent, which contained 3 g·L^{-1} of potassium trifluoroacetate (KOTFA) at a flow rate of 0.8 mL min^{-1} at 40°C. GPC columns were packed with modified silica (PFG-columns, particle size 7 µm, porosity 100 Å and 1000Å) purchased from Polymer Standards Service GmbH. Poly(methyl methacrylate) standards (Polymer Standards Service GmbH) and pSar standards were used for calibration and toluene was used as the internal standard.[62] A refractive index detector (G1362A RID, JASCO) and a UV detector (λ = 230nm, UV-2075+, JASCO) were used for polymer detection and analysis was performed using PSS WinGPC from PSS Polymer Standards Service GmbH.

Dynamic Light Scattering: Single-angle DLS measurements were performed with a ZetaSizer Nano ZS instrument (Malvern Instruments Ltd., Worcestershire, UK) equipped with a He-Ne laser (λ = 632.8 nm) as the incident beam. All measurements were performed at 25 °C and a detection angle of 173° unless

stated otherwise. Disposable polystyrene cuvettes (VWR, Darmstadt, Germany) were used for single-angle DLS measurements. Disposable folded capillary cells (Malvern Instruments Ltd., Worcestershire, UK) were employed for zeta potential measurements. Zeta potential measurements were conducted in solutions containing 3 mM sodium chloride. Cumulant size, polydispersity index (PDI), and size distribution (intensity weighted) histograms were calculated based on the autocorrelation function of the samples, with automated position and attenuator adjustment at multiple scans. The derived count rate was used for aggregation and dissociation experiments.

Thermogravimetric Analysis: TGA was performed on a Pyris 6 thermogravimetric analyzer (Perkin Elmer Inc.) using Pyris software. Analysis of lyophilized particle samples was performed in pure oxygen atmosphere at a heating rate of 10°C/minute from 50 to 800 °C. The mass concentration of iron was calculated from the residual iron oxide.

Atomic Force Microscopy: AFM was measured on mica using a Cypher AFM (Asylum Research) using tapping mode at a scan rate of 1 Hz. Samples were prepared by drop-casting of a particle solution ($\beta = 50$ mg $\cdot$L^{-1} in MilliQ water) onto freshly cleaned mica. The sample was dried overnight at room temperature. The AFM images were evaluated using Gwyddion 2.49.

Transmission Electron Microscopy: TEM was performed on a FEI Tecnai G2 Spirit microscope equipped with a Gatan US1000 2k x 2k CCD camera and LaB$_6$ cathode operated at 120 kV. Images were recorded using freshly glow discharged carbon coated copper grids (CF300-Cu, 300 mesh). For non-stained samples, 5 µL nanoparticle solution ($\beta = 50$ mg $\cdot$L^{-1} in MilliQ water) was drop-coated on the TEM grid surface and removed with a filter paper after 1 min. For negatively stained samples, 5 µL nanoparticle solution (b = 50 mg $\cdot$L^{-1} in MilliQ water) was drop-coated on the TEM grid, removed with a filter paper after 1 minute. Next, 5 µL uranyl acetate solution (2 wt.% in ethanol) were added and removed after 15 s incubation time. All sample-deposited grids were air-dried overnight before measurement. Software ImageJ 1.52h (National Institutes of Health, USA) was used for image evaluation.

For cryogenic TEM (CryoTEM), 5 µL of the nanoparticle solution (50 g L^{-1}, in MilliQ water) were applied to freshly glow-discharged carbon grids with a copper 200 mesh (Quantifoil Micro Tools GmbH). Excess fluid was removed by direct blotting (2.5 s) and the grids were individually plunge-frozen in liquid ethane.

Grids were cryotransferred in liquid nitrogen using a Gatan cryoholder (model 626 DH) to a Tecnai T12 transmission electron microscope equipped with a field emission electron source and operating at 120 kV accelerating voltage. Images were recorded using a TemCam-F416 (TVIPS, Gauting, Germany). Software ImageJ 1.52h (National Institutes of Health, USA) was used for image evaluation.

Magnetic Response: Images and videos of the magnetic response and particle guidance were recorded using digital single lens reflex cameras Nikon D90 and Nikon D750.

Magnetic data of SPION-CCPMs were collected with the help of a Quantum Design MPMS-XL-7 SQUID magnetometer on powdered sample. ZFC/FC experiment were recorded in a temperature range 4 to 300 K. The sample was cooled to 4 K before applying a field of 100 Oe. The sample was heated to 300 K and subsequent cooled to 4 K with a heating/cooling rate of 1 K /min. The maximum of the ZFC magnetization curve is at ca. 42 K. Below 44 K a splitting of the ZFC/FC magnetization curve can be observed. Magnetization data were collected at 5 and 300 K with magnetic fields up to 50000 Oe.

Fluorescence Correlation Spectroscopy: FCS measurements were performed using a commercial setup, a LSM 880 microscope (Carl Zeiss, Jena, Germany). For excitation of Cy5 an He/Ne-laser (633 nm) was used. The excitation light was focused into the sample by a C-Apochromat 40x/1.2 W (Carl, Zeiss, Jena, Germany) water immersion objective. The fluorescence light was collected with the same objective and after passing through a confocal pinhole, directed to a spectral detection unit (Quasar, Carl Zeiss). The detected emission range was in the spectral range of 642-696 nm. For calibration of the detection volume Atto Fluor643® was used, as a reference dye with known diffusion coefficient.

The measurements were performed in an eight-well polystyrene-chambered coverglass (Laboratory-Tek, Nalge Nunc Internation, Penfield, NY, USA). All samples were measured twenty times with a total duration of 3 minutes. The diffusion of the fluorescent particle through the confocal observation volume caused a time-dependent intensity fluctuation, which can be analysed by an autocorrelation function:

$$G(\tau) = 1 + \frac{\langle \delta I(t) \cdot \delta I(t+\tau) \rangle}{\langle I(t) \rangle^2} \tag{1}$$

For an ensemble of *m* different types of freely diffusion fluorescent species, $G(\tau)$ has the following form:[63]

$$G(\tau) = 1 + \frac{1}{N}\sum_{i=1}^{m}\frac{f_i}{\left(1+\frac{\tau}{\tau_{D,i}}\right)\cdot\sqrt{1+\frac{\tau}{S^2\cdot\tau_{D,i}}}} \tag{2}$$

N represents the average number of fluorescent species in the observation volume, $\tau_{D,i}$ is the diffusion time of the i-th species, f_i is the fraction of the i-th component and S is the so-called structure factor $S = \frac{z_0}{r_0}$, where z_0 and r_0 represent the axial and radial dimension of the confocal volume, respectively. The diffusion time $\tau_{D,i}$ relates to the diffusion coefficient D_i, through $D_i = \frac{r_0^2}{4\cdot\tau_{D,i}}$. The hydrodynamic radii R_h can be calculated using the Stokes-Einstein relation as $R_h = \frac{k_B\cdot T}{6\cdot\pi\cdot\eta\cdot D}$, where T is the absolute temperature, k_B the Boltzmann constant and η the viscosity of the solvent.

By fitting the experimental autocorrelation curves with Equation 2, we determined the hydrodynamic radii of the studied nanoparticles. Furthermore, their fluorescence brightness was also determined as $\langle I(t)\rangle/N$. To estimate the average number of Cy5 molecules per particle, the fluorescence brightness of the particles was divided by the fluorescence brightness of the Cy5 molecules.

Multi-Angle Dynamic Light Scattering: For multi-angle DLS cylindrical quartz cuvettes (Hellma, Mühlheim, Germany) were cleaned by dust-free distilled acetone and transferred to a dust free flow box. Light scattering measurements were performed on an ALV spectrometer consisting of a goniometer and an ALV-5004 multiple-tau full-digital correlator (320 channels) which allows measurements over an angular range from 30° to 150°. A He-Ne Laser (λ=632.8 nm) was used as light source. The correlation functions of the particles were fitted using a sum of two exponentials. The z-average diffusion coefficient D_z was calculated by extrapolating D_{app} for q = 0. By formal application of Stokes law, the inverse z-average hydrodynamic radius is $R_h= \langle R_h^{-1}\rangle_z^{-1}$ was determined. To investigate the aggregation behavior of the particles in human plasma, undiluted citrate plasma was filtered through a Millex GS 0.2 µm filter. The particle solutions were filtered through 0.45 µm pore size Millex LCR filters. The following mixtures were prepared from initial particle solutions in PBS (ß = 1 g·L⁻¹): PBS/particle solution 9:1 (ß = 0.1 g·L⁻¹), plasma/PBS 9:1 and plasma/particle solution 9:1 (ß = 0.1 g·L⁻¹). The cuvettes were incubated for 30 min at room temperature before measurement at T = 20°C. Data analysis was performed according to a procedure reported by Rausch *et al.*[47] The correlation functions of plasma were fitted with a triexponential decay function, while the particles were

fitted using a sum of two exponentials. Mixtures were fitted using a sum of both exponential decay functions with or without an additional aggregate term.

Polymer and Cross-Linker Synthesis: Polysarcosine-*block*-poly(*S*-ethylsulfonyl-L-cysteine) block copolymers were prepared by ring-opening *N*-carboxyanhydride (NCA) polymerization via bifunctional initiator approach, according to Scheme S1.[35] Results are summarized in Table S1. The synthesis of sarcosine NCA and *S*-ethylsulfonyl-L-cysteine NCA was performed as reported previously.[34,64]

Synthesis of Poly(sarcosine): Sarcosine NCA (3.00 g, 26.1 mmol, 200 eq.) was transferred into a pre-dried Schlenk-tube, dissolved in dry DMF (10 mL) and *N*-(*tert*-butoxycarbonyl)-1,2-diaminoethane (20.9 mg, 0.13 mmol, 1.0 eq.) was added *via* a stock solution in dry DMF. The clear, colorless solution was stirred at 10 °C in the absence of light until the reaction was completed after six days (as monitored by IR spectroscopy). The sarcosine amino terminus was quenched by addition perfluorophenyl 4-azidobutanoate (115 mg, 0.39 mmol, 3.0 eq) and *N*,*N*-diisopropylethylamine (133 µL, 0.78 mmol, 6.0 eq.). The reaction mixture was stirred overnight, followed by addition of acetic anhydride (134 µL, 1.30 mmol, 10 eq) and *N*,*N*-diisopropylethylamine (443 µL, 2.61 mmol, 20 eq.) to react residual end groups. The slightly yellow solution was stirred for an additional day at room temperature. Precipitation in diethyl ether yielded 1.82 g (97%) of a colorless solid. ^{1}H NMR (400 MHz, DMSO-d_6) δ [ppm] = 4.50-3.76 (m, 2nH, -CH_2-), 3.06-2.76 (m, 3nH, -CH_3), 1.37 (m, 9H, -OC(CH_3)$_3$). The chain length was determined by HFIP GPC relative to polysarcosine standards.[62]

The Boc protection group was removed in a mixture of water/trifluoro acetic acid (TFA) (1:1). The polymer (1.82g) was dissolved in water (32 mL), cooled with an ice bath, followed by addition of TFA (32 mL). After 4 h, the solution was transferred into a dialysis bag (MWCO 3.5 kDa) and dialyzed against MilliQ water, saturated sodium hydrogen carbonate solution, and MilliQ water. The aqueous solution was lyophilized, and the polymer was obtained as a colorless powder (1.65 g, 88%). ^{1}H NMR (400 MHz, DMSO-d_6) δ [ppm] = 4.50-3.76 (m, 2nH, -CH_2-), 3.06-2.76 (m, 3nH, -CH_3).

Synthesis of Poly(sarcosine)$_n$-block-poly(S-ethylsulfonyl-L-cysteine)$_m$: The poly-(sarcosine) macroinitiator (1.58 g, 0.138 mmol, 1.0 eq.) was weighed into a pre-dried Schlenk-tube and dried by azeotropic distillation with toluene in vacuo. The macroinitiator was dissolved in dry DMF (8.0 mL), cooled to -10 °C, and *S*-ethylsulfonyl-L-cysteine NCA (1.65 g, 6.90 mmol, 50 eq.) was added as a stock

solution in dry DMF. The polymerization was performed at a monomer concentration of β_{NCA} = 110 g·L⁻¹ and monitored by IR spectroscopy. After 2 days, the conversion was 63 % and the reaction was stopped by precipitation in THF. The suspension was centrifuged (4500 rpm, 15 min, 4°C) and decanted. This procedure was repeated twice concluding with pure diethyl ether. The product was dried in vacuo yielding poly(sarcosine)-*block*-poly(*S*-ethylsulfonyl-L-cysteine) (2.30 g, 79%) as a colorless solid. ¹H NMR (400 MHz, DMSO-d_6) δ [ppm] = 8.75 (b s, 1mH, N*H*CO), 4.69 (m, 1mH, α-*H*(Cys)), 4.49 - 3.78 (m, 2nH, -C*H*₂-(Sar)), 3.69 - 3.41 (m, 4mH, -C*H*₂S-, -SO₂C*H*₂-), 3.06 - 2.61 (m, 3nH, -C*H*₃(Sar)), 1.30 (t, 3mH, -C*H*₃(Cys)).

Synthesis of N-(3-azidopropyl)liponamide: The synthesis of *N*-(3-azidopropyl)-liponamide was performed similar to previous reports.[35]

Pentafluorophenol lipoate (260 mg, 698 µmol, 1.0 eq.) was weight into a pre-dried Schlenk flask and dissolved in absolute DMF (5.0 mL), before *N,N*-diisopropylethylamine (0.712 mL, 4.19 mmol, 6.0 eq.) and 3-azido-1-propanamine (76.8 mg, 768 µmol, 1.1 eq.) were added under nitrogen flow. The solution was stirred at room temperature for 16 h. The solvent was removed in vacuo and the reaction mixture was dissolved in dichloromethane (50 mL), washed with water (2 x 50 mL) and saturated NaHCO₃ solution (2 x 50 mL). The organic phase was dried over MgSO₄, filtered and concentrated under reduced pressure. The product purified by column chromatography using dichloromethane/methanol (2%) as eluent and obtained as a yellow liquid (180 mg, 0.625 mmol, 89 %). ¹H NMR (400 MHz, CDCl₃) δ [ppm] = 5.63 (s, 1H, -CON*H*-), 3.57 (dq, ^3J = 8.5 Hz, ^3J = 6.4 Hz, 1H, dq, -SC*H*-), 3.36 (m, 4H, -NHC*H*₂-,-C*H*₂N₃), 3.14 (m, 2H, -SC*H*₂-), 2.46 (m, 1H, -SC*H*₂C*H*₂-), 2.18 (td, ^3J = 7.4 Hz, ^3J = 1.2 Hz, 2H, α-C*H*₂), 1.91 (m, 1H, -SC*H*₂C*H*₂-), 1.80 (p, ^3J = 6.6 Hz, 2H, -C*H*₂CH₂N₃), 1.67 (m, 4H, ß-C*H*₂, δ-C*H*₂), 1.46 (m, 2H, γ-C*H*₂). ESI-MS m/z = 289.1 [M+H]⁺, ([M+H]⁺, (calc.) 289.1 g·mol⁻¹).

Synthesis of SPION-Loaded Core Cross-Linked Polymeric Micelles: Oleic acid-coated superparamagnetic iron oxide nanoparticles (SPIONs) (ß = 5.8 g L⁻¹, 9.0 mL) dispersed in hexanes were precipitated into 40 mL of ethanol, sonicated for 15 minutes and sedimented (4500 rpm, 15 min, 20°C). The pellet was resuspended in 5.0 mL of chloroform, sonicated for 30 minutes, precipitated in 45 mL of ethanol, and sedimented (4500 rpm, 15 min, 20°C) to remove excess oleic acid. SPIONs were resuspended in 20 mL of chloroform and a polymer solution in DMSO/CHCl₃ (1:2) (ß = 5.0 g L⁻¹, 10 mL) was added dropwise. The resulting clear

brown solution was placed in a dialysis bag (MWCO 3.5 kDa) and dialyzed against CHCl$_3$, followed by dialysis against DMSO. The solution was diluted with DMSO by factor 2 and dialyzed against MilliQ water to obtain SPION-loaded polymeric micelles. The obtained micelles were filtered through a PVDF 0.45 µm filter and concentrated to a total volume of 8.0 mL by spin filtration (Amicon Ultra-15, MWCO 3.0 kDa, 4500 rpm, 20°C). For core cross-linking, D,L-lipoic acid (8.0 mg, 39.1 mmol, 0.5 eq. per pCys(SO$_2$Et) repeating unit) was dissolved in ethanol (5.0 g L^{-1}) and treated with tris(2-carboxyethyl)phosphine hydrochloride (11.2 mg, 39.1 mmol, 50 g L^{-1} in MilliQ water) for 18 h yielding dihydro lipoic acid. The cross-linker solution was added to the micelle solution and the reaction mixture was placed on a benchtop shaker for 24 h. Subsequently, excess cross-linker and residual oleic acid were removed by dialysis (MWCO 3.5 kDa) against DMSO/MilliQ water mixtures (1:1) followed by dialysis against MilliQ water yielding a clear light brown solution. For dye conjugation, the SPION-CCPM solution was adjusted to pH 7.4 using 1 M sodium hydrogen carbonate solution, Cy5-NHS ester (540 µg, 0.3 eq. per polymer, 25 g L^{-1} in DMSO) was added, and the solution was stirred at room temperature for 72 h. Upon addition of the blue dye solution, the particle solution turned dark green immediately. The excess dye was removed by repetitive extraction with dichloromethane, followed by dialysis against ethanol/MilliQ water mixtures (1:1) and MilliQ water (MWCO 6-8 kDa). To remove the free polymer, Cy5-labelled SPION-loaded core cross-linked polymeric micelles (SPION-CCPM^{Cy5}) were purified by repetitive spin filtration (Amicon Ultra-15, MWCO 100 kDa, 3000 rpm, 20°C), and finally concentrated to a total volume of 8.5 mL, yielding 23 mg of SPION-CCPM^{Cy5} (overall yield 23%).

Synthesis of Core Cross-Linked Polymeric Micelles (Control-Particles): The preparation of core cross-linked polymeric micelles was performed as described previously.[35,37]

Poly(sarcosine)-*block*-poly(*S*-ethylsulfonyl-L-cysteine) (pSar$_{225}$-*b*-pCys(SO$_2$Et)$_{31}$) was dissolved in dimethyl sulfoxide (DMSO) equipped with 1 M thiourea at a concentration of 7.5 g·L^{-1} for 1 h. Next, 20 vol.% of 1 mM acetate buffer (pH 4.75) with 10 mM thiourea were added to adjust the concentration to 6.6 g·L^{-1}. The solution was left to equilibrate at room temperature for 5 h, followed by dialysis against 1 mM acetate buffer (pH 4.75) with 10 mm thiourea. The solution was filtered (GHP 450) and concentrated to 6.6 g·L^{-1} by spin filtration (Amicon Ultra, MWCO 3 kDa), yielding the micelle solution. For cross-linking, in a separate flask, *N*-3-azidopropyl liponamide was dissolved in ethanol at a concentration of ß =

$10 \ g \cdot L^{-1}$ and one equivalent of an aqueous solution of tris(2-carboxyethyl)phosphine hydrochloride (TCEP·HCl) ($50 \ g \cdot L^{-1}$) was added per disulfide. After 18 h, the cross-linker solution was added to the micelle solution at equimolar amounts of thiols per cysteines. The reaction mixture was allowed to stand at room temperature for 48 h. To remove residual cross-linker and free polymer, the solution was dialyzed against DMSO and MilliQ water (MWCO 6-8 kDa), followed by repetitive spin filtration (Amicon Ultra, MWCO 100 kDa). For labelling, the pH was adjusted to 7.4 (1 m NaHCO$_3$ solution) and 0.3 equivalents of Cyanine 5-NHS-ester stock solution in DMSO ($25 \ g \cdot L^{-1}$) were added per polymer end-group. After 72 h, excess dye was removed by repetitive spin filtration (Amicon Ultra, 100 kDa) using ethanol/water mixtures and the final particle solution (in MilliQ water) was stored at 4°C. The absence of free polymer and free dye was verified by gel permeation chromatography in hexafluoro isopropanol.

Isolation of Bone Marrow-Derived Macrophages: The procedure conducted follows previously established protocol.[65] Briefly, bone marrow cells were flushed from the tibia and femurs of C57BL/6N wild-type mice (8-10 weeks of age) using ice cold HBSS, filtered through a 70 µm filter cell strainer and plated at a density of $3.5 \ x \ 10^5$ cells/ml. Cells were differentiated for one-week using RPMI medium supplemented with 10 ng/mL M-CSF (M9170, Sigma-Aldrich), 10 % fetal bovine serum (FBS) and 1 % penicillin/streptomycin (Gibco). For each independent experiment, BMDMs were prepared from three different mice.

Cell Lines: LLC cells were regularly tested for mycoplasma contamination and authenticated by visual observations of cell morphology. Cells were cultured in Roswell Park Memorial Institute Medium (RPMI, Life Technologies) containing 10 % FBS and 1 % penicillin/streptomycin.

Hepatocyte Isolation: Hepatocytes from C57BL/6N wild-type mice (8-10 weeks of age) were prepared following a standard two-step perfusion method.[66–68] Briefly, liver perfusion (Life Technologies #17701038) and liver digest medium (Life Technologies #17703-034) were pumped into the liver through the cava vein with a $5 \ mL \cdot min^{-1}$ flux rate. The liver capsule was mechanically disrupted in hepatocyte wash medium (Life Technologies #17704-024). The cell suspension obtained was passed through 100 µm filter and centrifuged for 5 minutes at 50 G and 4°C. The pellet of hepatocytes was resuspended in William's E medium (Life Technologies #32551-020) supplemented with 4% FBS and $2.50 \ x \ 10^5$ cells·mL^{-1}

were plated on 13 mm collagen-coated (Life Technologies #A1048301) glass cover slips.

Mice: 10 female C57Bl/6 mice, aged 6-8 weeks, were housed in specific pathogen-free conditions under constant light-dark cycle and maintained on a standard mouse diet. Experimentation was performed at the DKFZ animal facilities, in accordance with institutional guidelines, and were approved by the Regierungspräsidium Karlsruhe, Germany, under permit number G214/19. Mice were anaesthetized by intraperitoneal injection of 100 µg·g^{-1} ketamine and 14 µg·g^{-1} xylazine and intratracheally instilled with SPION-CCPM (10 mg·kg^{-1} of iron to body weight) or PBS in a final volume of 50 µL.

Immunofluorescence: BMDMs were plated on 13 mm collagen-coated (Life Technologies #A1048301) glass cover slips in a density of 1.0×10^5 cells/slip. After treatment, cells were washed three times with phosphate-buffered saline (PBS) and fixed with 4% paraformaldehyde for 15 minutes at room temperature. Cells were then washed three times with PBS and blocked with 2.5% milk in PBS-T (0.1% Tween) solution for 30 minutes on an orbital shaker. Slips were then washed three times with 0.1% PBS-T and incubated with primary antibody Iba1 (NB100-1028SS, Bio Techne) overnight at 4°C or 1 hour at room temperature. After washing with PBS-T, samples were incubated with secondary antibody (A-11057, Donkey anti-Goat IgG (H+L) Cross-adsorbed Secondary Antibody Alexa Fluor 568, Life Technologies) for 1 hour at room temperature. Slips were then washed with PBS and mounted using Prolong Gold Antifade Mountant with DAPI (P36931, Life Technologies). Samples were acquired at the University of Heidelberg Nikon Imaging Centre using a Ni-E confocal microscope. Images were analysed using Fiji (National Institute for Health) using a written macro for intracellular quantification of the Cy5+ signal. Images were compiled into figures using Adobe Photoshop and Illustrator.

Flow Cytometry: Mouse lungs were resected and washed in PBS. Single cell suspensions (200 µL) were generated by applying chemical and mechanical digestion using the Miltenyi Lung Dissociation Kit and pelleted by centrifugation for 5 mins at 300G. Cells were then washed with FACS Buffer (1% fetal bovine serum, 2.5 mM 1M HEPES, 1 mM EDTA) prior to antibody staining. Cells were stained with anti-mouse CD45-PERCPCy5.5 (BD Biosciences), LY6G-FITC (BioLegend, California, USA), LY6C-PEDAZZLE (BD Biosciences), F4/80-BV605 (BioLegend, California, USA), CD11C-PE (BioLegend, California, USA),

SIGLECF-APCCY7 (BD Biosciences), CD11B-PERCP (BD Biosciences), CD64-BV711 (BioLegend, California, USA), CD80-BV650 (BioLegend, California, USA), CD71-BV510 (BioLegend, California, USA), MERTK-BV421 (BD Biosciences) and the viability stain DAPI (BioLegend, California, USA). Samples were acquired using Cytotek Aurora flow cytometer at the EMBL Flow Cytometry Core Facility and analysis was performed using the FlowJo Software (Tree Star Inc).

BMDMs were incubated with Fc-γ receptor blocking solution and stained with anti-mouse CD206-FITC, CD86-PE, MHC II-PeCy5 (BioLegend, California, USA), CD301-PerCPCy5.5, CD38-FITC (BD Biosciences) and the viability staining solution 7AAD (420404, Biozol) (see Table S3). Data were acquired using a FACS Fortessa (BD, Biosciences) or Cytotek Aurora flow cytometer at the EMBL Flow Cytometry Core Facility and analysis was performed using the FlowJo Software (Tree Star Inc). The expression of surface markers in mouse lung cells and BMDM was calculated by subtracting the geometric median fluorescence intensity (MFI) of cells stained with the isotype-matched antibody from the MFI of those stained with the specific antibody and is shown as fold-change compared to the non-treated (NT) control.

Tissue Non-Heme Iron Measurement: Lungs of mice were measured for non-heme iron content using the bathophenantroline method and calculated against dry weight of tissue.[69]

Cytotoxicity: BMDM viability was quantified using CytoTox96 kit from Promega. Cells were plated in a black side/black bottom 96 well plate at a concentration of 10,000 cells in 100 µL/well 24 hours before start of the experiment. To measure LDH release into the supernatant, plate was centrifuged at 500 G for 10 mins to sediment cells and 100 µL was transferred to a new 96 well plate. 50 µL of substrate was added to 50 µL of supernatant and incubated for 30 minutes at room temperature in the dark. After 30 minutes, 20 µL stop solution was added to each well and the 490 nm signal was measured in a spectrofluorimeter (SpectraMax, Molecular Devices). Viability was calculated by subtracting the media blank from experimental values and normalized to the non-treated condition (NT). To measure redox capacity, after incubation times with conditions, 10 µL of Celltiter Blue was added to each well and plate was incubated at 37°C for 4 hours. Absorbance was then measured at 520 nm and all values were subtracted from the media blank control and normalized to the non-treated condition (NT).

RNA extraction, Reverse Transcription, and Quantitative Real-Time Polymerase Chain Reaction Analysis: RNA was extracted from lung tissue using Trizol (Life Technologies). RNA was extracted from BMDMS using the RNeasy Mini Kit (74134, Qiagen). 0.5 to 1 µg of total RNA was reverse transcribed by using RevertAid H Minus Reverse Transcriptase (FERMEP0452, Thermo Scientific), random primers (48190-011, Invitrogen) and dNTPs (R0193, ThermoScientific). SYBR green qRT-PCR was performed on a Step One Plus Real Time PCR System (Applied Biosystems, California, USA). Primers and probes were designed using the ProbeFinder software (www.roche-applied-science.com) (See Table S4). Differences in Relative Quantity (RQ) are shown as fold-change compared to the control condition (untreated cells, NT).

Measurement of Intracellular ROS Accumulation: Accumulation of ROS in BMDM cells was assessed by using the oxidant-sensitive fluorescent dye CELLROX™ Green and CELLROX™ Orange (Life Technologies). Upon cellular uptake, the non-fluorescent CELLROX™ probe undergoes deacetylation by intracellular esterases producing a highly green fluorescent signal following oxidation by intracellular ROS. BMDMs were maintained untreated or were treated for 4 or 18 hours with 20 µM SPION-CCPMs, CCPMs, 100 ng·mL^{-1} lipopolysaccharide (LPS) or interferon-γ, 20 µM ferric ammonium citrate (FAC), or 20 µM heme. The amount of SPION-CCPMs added to cells was calculated to 20 µM iron from within the core. Then the amount of CCPMs added to cells was calculated to match the mass of CCPMs contained within added SPION-CCPMs. 2.5 mM of CELLROX™ Green or Orange was added to cells and incubated for 30 minutes at 37 °C under 5% CO_2 atmosphere. Cells were washed twice with Hanks' Balanced Salt Solution (HBSS) and fluorescence intensity was measured using FACS. Fluorescence intensity is represented as fold change compared to the non-treated condition (NT).

Protein Extraction and Western Blotting: Protein lysates were obtained by homogenizing cells in RIPA buffer supplemented with protease inhibitors (Roche Diagnostics). Protein concentration was determined using the DC™ Protein Assay Kit II system (5000112, Bio-Rad, München, Germany). 50 µg of total protein extracts were separated by 12% SDS-PAGE and analyzed by Western blotting using antibodies against HO-1 (Stressgen, Victoria, Canada) or TfR1 (136800, Invitrogen/Life Tech). ß-actin (A1978-200UL, Sigma-Aldrich) was used as a loading control. Densitometric analysis is reported in Arbitrary Unit (AU), as ratio to the untreated (NT) sample (AU=1). Western blot images were

quantitatively acquired with the Vilber Lourmat Fusion-FX Chemiluminescence system (Eberhardzell).

Pearls' Prussian Blue Staining: 3.5×10^5 BMDMs were plated on a 13 mm (Life Technologies #A1048301) glass slips. After incubation or treatment, cells were washed three times with PBS and fixed with 4% paraformaldehyde at room temperature for ten minutes. Cells were then washed three times with PBS and stained with Accustain Iron Stain No. HT20 (Sigma-Aldrich) following manufacturer's instructions and counterstained with Fast Red (Sigma Aldrich). Samples were mounted using the water-soluble mounting agent VectaMount (H5501, Biozol). Images were digitally acquired with a Nikon Ni-E microscope, using the Nikon NIS-Elements Viewer software and assembled into figures using Adobe Photoshop and Illustrator software packages.

Buffy Coat Preparation: Human monocytes were isolated from commercially available buffy coats (DRK-Blutspendedienst Baden-Württemberg-Hessen, Frankfurt, Germany) using Ficoll-Hypaque gradients (LSM-1077; PAA Laboratories). Monocytes were differentiated into primary human macrophages with RPMI 1640 containing 5% AB-positive human serum (DRK-Blutspendedienst) for 7 days and achieved approximately 80% confluence. 24 hours prior to stimulation, cells were serum starved. Cells were then prepared to analyze cell surface expression of proteins by FACS measurement (antibodies in Table S3) or differential mRNA expression by qPCR (primers in Table S5).

Statistical Analysis: Data are shown as mean ± SEM. Statistical analyses were performed using Prims v10 (GraphPad Software, La Jolla, CA). One-way ANOVA was used and p-values < 0.05 (*), < 0.01 (**), < 0.001 (***) and < 0.0001 (****) are indicated.

Acknowledgement

Conflict of Interest

T.A.B., N.K.H., M.U.M., M.W.H., and M.B. have submitted the patent application "SPION-CCPM; Nanoparticles Comprising Iron Oxide Particles Embedded in Polymeric Micelles" EP20210176.2.

References

(1)   Costa da Silva, M.; Breckwoldt, M. O.; Vinchi, F.; Correia, M. P.; Stojanovic, A.; Thielmann, C. M.; Meister, M.; Muley, T.; Warth, A.; Platten, M.; Hentze, M. W.; Cerwenka, A.; Muckenthaler, M. U. Iron Induces Anti-Tumor Activity in Tumor-Associated Macrophages. *Front. Immunol.* **2017**, *8* (November).

(2)   Ardura, J. A.; Rackov, G.; Izquierdo, E.; Alonso, V.; Gortazar, A. R.; Escribese, M. M. Targeting Macrophages: Friends or Foes in Disease? *Front. Pharmacol.* **2019**, *10* (October), 1–8.

(3)   Chinetti-Gbaguidi, G.; Staels, B. Macrophage Polarization in Metabolic Disorders. *Curr. Opin. Lipidol.* **2011**, *22* (5), 365–372.

(4)   Tangudu, N. K.; Alan, B.; Vinchi, F.; Wörle, K.; Lai, D.; Vettorazzi, S.; Leopold, K.; Vujić Spasić, M. Scavenging Reactive Oxygen Species Production Normalizes Ferroportin Expression and Ameliorates Cellular and Systemic Iron Disbalances in Hemolytic Mouse Model. *Antioxid. Redox Signal.* **2018**, *29* (5), 484–499.

(5)   Ruffell, B.; Coussens, L. M. Macrophages and Therapeutic Resistance in Cancer. *Cancer Cell* **2015**, *27* (4), 462–472.

(6)   Murray, P. J. Macrophage Polarization. *Annu. Rev. Physiol.* **2017**, *79*, 541–566.

(7)   Cairo, G.; Recalcati, S.; Mantovani, A.; Locati, M. Iron Trafficking and Metabolism in Macrophages: Contribution to the Polarized Phenotype. *Trends Immunol.* **2011**, *32* (6), 241–247.

(8)   Bao, Y.; Sherwood, J. A.; Sun, Z. Magnetic Iron Oxide Nanoparticles as: T 1 Contrast Agents for Magnetic Resonance Imaging. *J. Mater. Chem. C* **2018**, *6* (6), 1280–1290.

(9)   Mebius, R. E.; Kraal, G. Structure and Function of the Spleen. *Nat. Rev. Immunol.* **2005**, *5* (8), 606–616.

(10)   Sica, A.; Mantovani, A. Macrophage Plasticity and Polarization: In Vivo Veritas. *J. Clin. Invest.* **2012**, *122* (3), 787–795.

(11)   Lewis, C. E.; Pollard, J. W. Distinct Role of Macrophages in Different Tumor

Microenvironments. *Cancer Res.* **2006**, *66* (2), 605–612.

(12)   Guerriero, J. L. Macrophages: The Road Less Traveled, Changing Anticancer Therapy. *Trends Mol. Med.* **2018**, *24* (5), 472–489.

(13)   Davra, V.; Kimani, S.; Calianese, D.; Birge, R. Ligand Activation of TAM Family Receptors-Implications for Tumor Biology and Therapeutic Response. *Cancers (Basel).* **2016**, *8* (12), 107.

(14)   Recalcati, S.; Locati, M.; Marini, A.; Santambrogio, P.; Zaninotto, F.; De Pizzol, M.; Zammataro, L.; Girelli, D.; Cairo, G. Differential Regulation of Iron Homeostasis during Human Macrophage Polarized Activation. *Eur. J. Immunol.* **2010**, *40* (3), 824–835.

(15)   Sukhbaatar, N.; Weichhart, T. Iron Regulation: Macrophages in Control. *Pharmaceuticals* **2018**, *11* (4), 137.

(16)   Hentze, M. W.; Muckenthaler, M. U.; Galy, B.; Camaschella, C. Two to Tango: Regulation of Mammalian Iron Metabolism. *Cell* **2010**, *142* (1), 24–38.

(17)   Muckenthaler, M. U.; Rivella, S.; Hentze, M. W.; Galy, B. A Red Carpet for Iron Metabolism. *Cell* **2017**, *168* (3), 344–361.

(18)   Vinchi, F.; Costa da Silva, M.; Ingoglia, G.; Petrillo, S.; Brinkman, N.; Zuercher, A.; Cerwenka, A.; Tolosano, E.; Muckenthaler, M. U. Hemopexin Therapy Reverts Heme-Induced Proinflammatory Phenotypic Switching of Macrophages in a Mouse Model of Sickle Cell Disease. *Blood* **2016**, *127* (4), 473–486.

(19)   Zanganeh, S.; Hutter, G.; Spitler, R.; Lenkov, O.; Mahmoudi, M.; Shaw, A.; Pajarinen, J. S.; Nejadnik, H.; Goodman, S.; Moseley, M.; Coussens, L. M.; Daldrup-Link, H. E. Iron Oxide Nanoparticles Inhibit Tumour Growth by Inducing Pro-Inflammatory Macrophage Polarization in Tumour Tissues. *Nat. Nanotechnol.* **2016**, *11* (11), 986–994.

(20)   Wang, G.; Zhao, J.; Zhang, M.; Wang, Q.; Chen, B.; Hou, Y.; Lu, K. Ferumoxytol and CpG Oligodeoxynucleotide 2395 Synergistically Enhance Antitumor Activity of Macrophages against NSCLC with EGFRL858R/T790M Mutation. *Int. J. Nanomedicine* **2019**, *14*, 4503–4515.

(21)   Zhao, J.; Zhang, Z.; Xue, Y.; Wang, G.; Cheng, Y.; Pan, Y.; Zhao, S.; Hou, Y. Anti-Tumor Macrophages Activated by Ferumoxytol Combined or Surface-Functionalized with the TLR3 Agonist Poly (I : C) Promote Melanoma Regression. *Theranostics* **2018**, *8* (22), 6307–6321.

(22)   Jin, R.; Liu, L.; Zhu, W.; Li, D.; Yang, L.; Duan, J.; Cai, Z.; Nie, Y.; Zhang, Y.; Gong, Q.; Song, B.; Wen, L.; Anderson, J. M.; Ai, H. Iron Oxide Nanoparticles Promote Macrophage Autophagy and Inflammatory Response through Activation of Toll-like Receptor-4 Signaling. *Biomaterials* **2019**, *203*, 23–30.

(23)   Trujillo-Alonso, V.; Pratt, E. C.; Zong, H.; Lara-Martinez, A.; Kaittanis, C.; Rabie, M. O.; Longo, V.; Becker, M. W.; Roboz, G. J.; Grimm, J.; Guzman, M. L. FDA-Approved Ferumoxytol Displays Anti-Leukaemia Efficacy against Cells with Low Ferroportin Levels. *Nat. Nanotechnol.* **2019**, *14* (6), 616–622.

(24)   El-Boubbou, K. Magnetic Iron Oxide Nanoparticles as Drug Carriers: Clinical Relevance. *Nanomedicine* **2018**, *13* (8), 953–971.

(25)   Balakrishnan, V. S.; Rao, M.; Kausz, A. T.; Brenner, L.; Pereira, B. J. G.; Frigo, T. B.; Lewis, J. M. Physicochemical Properties of Ferumoxytol, a New Intravenous Iron

Preparation. *Eur. J. Clin. Invest.* **2009**, *39* (6), 489–496.

(26) EMA. *Rienso Withdrawal of the Marketing Authorization in the European Union*; EMA/43791/2015; 2015.

(27) Dadfar, S. M.; Roemhild, K.; Drude, N. I.; von Stillfried, S.; Knüchel, R.; Kiessling, F.; Lammers, T. Iron Oxide Nanoparticles: Diagnostic, Therapeutic and Theranostic Applications. *Adv. Drug Deliv. Rev.* **2019**, *138*, 302–325.

(28) Weissleder, R.; Stark, D.; Engelstad, B.; Bacon, B.; Compton, C.; White, D.; Jacobs, P.; Lewis, J. Superparamagnetic Iron Oxide: Pharmacokinetics and Toxicity. *Am. J. Roentgenol.* **1989**, *152* (1), 167–173.

(29) Lu, M.; Cohen, M. H.; Rieves, D.; Pazdur, R. FDA Report: Ferumoxytol for Intravenous Iron Therapy in Adult Patients with Chronic Kidney Disease. *Am. J. Hematol.* **2010**, *85* (5), NA-NA.

(30) Toth, G. B.; Varallyay, C. G.; Horvath, A.; Bashir, M. R.; Choyke, P. L.; Daldrup-Link, H. E.; Dosa, E.; Finn, J. P.; Gahramanov, S.; Harisinghani, M.; Macdougall, I.; Neuwelt, A.; Vasanawala, S. S.; Ambady, P.; Barajas, R.; Cetas, J. S.; Ciporen, J.; DeLoughery, T. J.; Doolittle, N. D.; Fu, R.; Grinstead, J.; Guimaraes, A. R.; Hamilton, B. E.; Li, X.; McConnell, H. L.; Muldoon, L. L.; Nesbit, G.; Netto, J. P.; Petterson, D.; Rooney, W. D.; Schwartz, D.; Szidonya, L.; Neuwelt, E. A. Current and Potential Imaging Applications of Ferumoxytol for Magnetic Resonance Imaging. *Kidney Int.* **2017**, *92* (1), 47–66.

(31) Birke, A.; Ling, J.; Barz, M. Polysarcosine-Containing Copolymers: Synthesis, Characterization, Self-Assembly, and Applications. *Prog. Polym. Sci.* **2018**, *81*, 163–208.

(32) Klinker, K.; Barz, M. Polypept(o)Ides: Hybrid Systems Based on Polypeptides and Polypeptoids. *Macromol. Rapid Commun.* **2015**, *36* (22), 1943–1957.

(33) Sevier, C. S.; Kaiser, C. A. Formation and Transfer of Disulphide Bonds in Living Cells. *Nat. Rev. Mol. Cell Biol.* **2002**, *3* (11), 836–847.

(34) Birke, A.; Huesmann, D.; Kelsch, A.; Weilbächer, M.; Xie, J.; Bros, M.; Bopp, T.; Becker, C.; Landfester, K.; Barz, M. Polypeptoid- Block -Polypeptide Copolymers: Synthesis, Characterization, and Application of Amphiphilic Block Copolypept(o)ides in Drug Formulations and Miniemulsion Techniques. *Biomacromolecules* **2014**, *15* (2), 548–557.

(35) Klinker, K.; Schäfer, O.; Huesmann, D.; Bauer, T.; Capelôa, L.; Braun, L.; Stergiou, N.; Schinnerer, M.; Dirisala, A.; Miyata, K.; Osada, K.; Cabral, H.; Kataoka, K.; Barz, M. Secondary-Structure-Driven Self-Assembly of Reactive Polypept(o)Ides: Controlling Size, Shape, and Function of Core Cross-Linked Nanostructures. *Angew. Chemie Int. Ed.* **2017**, *56* (32), 9608–9613.

(36) Talelli, M.; Barz, M.; Rijcken, C. J. F. F.; Kiessling, F.; Hennink, W. E.; Lammers, T. Core-Crosslinked Polymeric Micelles: Principles, Preparation, Biomedical Applications and Clinical Translation. *Nano Today* **2015**, *10* (1), 93–117.

(37) Dal, N. K.; Kocere, A.; Wohlmann, J.; Van Herck, S.; Bauer, T. A.; Resseguier, J.; Bagherifam, S.; Hyldmo, H.; Barz, M.; De Geest, B. G.; Fenaroli, F. Zebrafish Embryos Allow Prediction of Nanoparticle Circulation Times in Mice and Facilitate Quantification of Nanoparticle–Cell Interactions. *Small* **2020**, *16* (5), 1906719.

(38) Ojha, T.; Hu, Q.; Colombo, C.; Wit, J.; Geijn, M.; Steenbergen, M. J.; Bagheri, M.;

Königs-Werner, H.; Buhl, E. M.; Bansal, R.; Shi, Y.; Hennink, W. E.; Storm, G.; Rijcken, C. J. F.; Lammers, T. Lyophilization Stabilizes Clinical-stage Core-crosslinked Polymeric Micelles to Overcome Cold Chain Supply Challenges. *Biotechnol. J.* **2021**, *16* (6), 2000212.

(39) Kim, B.-S.; Qiu, J.-M.; Wang, J.-P.; Taton, T. A. Magnetomicelles: Composite Nanostructures from Magnetic Nanoparticles and Cross-Linked Amphiphilic Block Copolymers. *Nano Lett.* **2005**, *5* (10), 1987–1991.

(40) Talelli, M.; Rijcken, C. J. F.; Lammers, T.; Seevinck, P. R.; Storm, G.; van Nostrum, C. F.; Hennink, W. E. Superparamagnetic Iron Oxide Nanoparticles Encapsulated in Biodegradable Thermosensitive Polymeric Micelles: Toward a Targeted Nanomedicine Suitable for Image-Guided Drug Delivery. *Langmuir* **2009**, *25* (4), 2060–2067.

(41) Schmidtke, C.; Eggers, R.; Zierold, R.; Feld, A.; Kloust, H.; Wolter, C.; Ostermann, J.; Merkl, J. P.; Schotten, T.; Nielsch, K.; Weller, H. Polymer-Assisted Self-Assembly of Superparamagnetic Iron Oxide Nanoparticles into Well-Defined Clusters: Controlling the Collective Magnetic Properties. *Langmuir* **2014**, *30* (37), 11190–11196.

(42) Amstad, E.; Zurcher, S.; Mashaghi, A.; Wong, J. Y.; Textor, M.; Reimhult, E. Surface Functionalization of Single Superparamagnetic Iron Oxide Nanoparticles for Targeted Magnetic Resonance Imaging. *Small* **2009**, *5* (11), 1334–1342.

(43) Karaoğlu, E.; Baykal, A.; Erdemi, H.; Alpsoy, L.; Sozeri, H. Synthesis and Characterization of Dl-Thioctic Acid (DLTA)–Fe3O4 Nanocomposite. *J. Alloys Compd.* **2011**, *509* (37), 9218–9225.

(44) Demortière, A.; Panissod, P.; Pichon, B. P.; Pourroy, G.; Guillon, D.; Donnio, B.; Bégin-Colin, S. Size-Dependent Properties of Magnetic Iron Oxidenanocrystals. *Nanoscale* **2011**, *3* (1), 225–232.

(45) Baun, O.; Blümler, P. Permanent Magnet System to Guide Superparamagnetic Particles. *J. Magn. Magn. Mater.* **2017**, *439*, 294–304.

(46) Kawasaki, R.; Sasaki, Y.; Katagiri, K.; Mukai, S.; Sawada, S.; Akiyoshi, K. Magnetically Guided Protein Transduction by Hybrid Nanogel Chaperones with Iron Oxide Nanoparticles. *Angew. Chemie* **2016**, *128* (38), 11549–11553.

(47) Rausch, K.; Reuter, A.; Fischer, K.; Schmidt, M. Evaluation of Nanoparticle Aggregation in Human Blood Serum. *Biomacromolecules* **2010**, *11* (11), 2836–2839.

(48) Koynov, K.; Butt, H. J. Fluorescence Correlation Spectroscopy in Colloid and Interface Science. *Curr. Opin. Colloid Interface Sci.* **2012**, *17* (6), 377–387.

(49) Mahmoudi, M.; Sant, S.; Wang, B.; Laurent, S.; Sen, T. Superparamagnetic Iron Oxide Nanoparticles (SPIONs): Development, Surface Modification and Applications in Chemotherapy. *Adv. Drug Deliv. Rev.* **2011**, *63* (1–2), 24–46.

(50) Michelet, F.; Gueguen, R.; Leroy, P.; Wellman, M.; Nicolas, A.; Siest, G. Blood and Plasma Glutathione Measured in Healthy Subjects by HPLC: Relation to Sex, Aging, Biological Variables, and Life Habits. *Clin. Chem.* **1995**, *41* (10), 1509–1517.

(51) Ahmed, S. M. U.; Luo, L.; Namani, A.; Wang, X. J.; Tang, X. Nrf2 Signaling Pathway: Pivotal Roles in Inflammation. *Biochim. Biophys. Acta - Mol. Basis Dis.* **2017**, *1863* (2), 585–597.

(52) Shenoy, N.; Stenson, M.; Lawson, J.; Abeykoon, J.; Patnaik, M.; Wu, X.; Witzig, T.

Drugs with Anti-Oxidant Properties Can Interfere with Cell Viability Measurements by Assays That Rely on the Reducing Property of Viable Cells. *Lab. Investig.* **2017**, *97* (5), 494–497.

(53) Thielmann, C. M.; Costa da Silva, M.; Muley, T.; Meister, M.; Herpel, E.; Muckenthaler, M. U. Iron Accumulation in Tumor-Associated Macrophages Marks an Improved Overall Survival in Patients with Lung Adenocarcinoma. *Sci. Rep.* **2019**, *9* (1), 11326.

(54) Ponzoni, M.; Pastorino, F.; Di Paolo, D.; Perri, P.; Brignole, C. Targeting Macrophages as a Potential Therapeutic Intervention: Impact on Inflammatory Diseases and Cancer. *Int. J. Mol. Sci.* **2018**, *19* (7), 1953.

(55) Lee, W.-H.; Loo, C.-Y.; Traini, D.; Young, P. M. Nano- and Micro-Based Inhaled Drug Delivery Systems for Targeting Alveolar Macrophages. *Expert Opin. Drug Deliv.* **2015**, *12* (6), 1009–1026.

(56) Shah, D. P. Fundamentals of Nanocarriers and Drug Targeting. In *Nanocarriers: Drug Delivery System*; Springer Singapore: Singapore, 2021; pp 3–42.

(57) Chakraborty, A.; Royce, S.; Selomulya, C.; Plebanski, M. A Novel Approach for Non-Invasive Lung Imaging and Targeting Lung Immune Cells. *Int. J. Mol. Sci.* **2020**, *21* (5), 1613.

(58) Shi, T.; Denney, L.; An, H.; Ho, L.; Zheng, Y. Alveolar and Lung Interstitial Macrophages: Definitions, Functions, and Roles in Lung Fibrosis. *J. Leukoc. Biol.* **2020**, JLB.3RU0720-418R.

(59) Bedoret, D.; Wallemacq, H.; Marichal, T.; Desmet, C.; Quesada Calvo, F.; Henry, E.; Closset, R.; Dewals, B.; Thielen, C.; Gustin, P.; de Leval, L.; Van Rooijen, N.; Le Moine, A.; Vanderplasschen, A.; Cataldo, D.; Drion, P.-V.; Moser, M.; Lekeux, P.; Bureau, F. Lung Interstitial Macrophages Alter Dendritic Cell Functions to Prevent Airway Allergy in Mice. *J. Clin. Invest.* **2009**, *119* (12), 3723–3738.

(60) Cai, B.; Kasikara, C.; Doran, A. C.; Ramakrishnan, R.; Birge, R. B.; Tabas, I. MerTK Signaling in Macrophages Promotes the Synthesis of Inflammation Resolution Mediators by Suppressing CaMKII Activity. *Sci. Signal.* **2018**, *11* (549), eaar3721.

(61) Ulich, T. R.; Watson, L. R.; Yin, S.; Guo, K.; Wang, P.; Thang, H.; Del Castillo, J. The Intratracheal Administration of Endotoxin and Cytokines: I. Characterization of LPS-Induced IL-1 and TNF MRNA Expression and the LPS-, IL-1-, and TNF-Induced Inflammatory Infiltrate. *Am. J. Pathol.* **1991**, *138* (6), 1485–1496.

(62) Weber, B.; Birke, A.; Fischer, K.; Schmidt, M.; Barz, M. Solution Properties of Polysarcosine: From Absolute and Relative Molar Mass Determinations to Complement Activation. *Macromolecules* **2018**, *51* (7), 2653–2661.

(63) Rigler, R.; Elson, E. S. *Fluorescence Correlation Spectroscopy: Theory and Applications*; Springer Series in Chemical Physics; Springer Berlin, 2012.

(64) Schäfer, O.; Huesmann, D.; Muhl, C.; Barz, M. Rethinking Cysteine Protective Groups: S -Alkylsulfonyl- l -Cysteines for Chemoselective Disulfide Formation. *Chem. - A Eur. J.* **2016**, *22* (50), 18085–18091.

(65) Guida, C.; Altamura, S.; Klein, F. A.; Galy, B.; Boutros, M.; Ulmer, A. J.; Hentze, M. W.; Muckenthaler, M. U. A Novel Inflammatory Pathway Mediating Rapid Hepcidin-Independent Hypoferremia. *Blood* **2015**, *125* (14), 2265–2275.

(66) Klaunig, J. E.; Goldblatt, P. J.; Hinton, D. E.; Lipsky, M. M.; Trump, B. F. Mouse

Liver Cell Culture. I. Hepatocyte Isolation. *In Vitro* **1981**, *17* (10), 913–925.

(67)   Klaunig, J. E.; Goldblatt, P. J.; Hinton, D. E.; Lipsky, M. M.; Trump, B. F. Mouse Liver Cell Culture. II. Primary Culture. *In Vitro* **1981**, *17* (10), 926–934.

(68)   Severgnini, M.; Sherman, J.; Sehgal, A.; Jayaprakash, N. K.; Aubin, J.; Wang, G.; Zhang, L.; Peng, C. G.; Yucius, K.; Butler, J.; Fitzgerald, K. A Rapid Two-Step Method for Isolation of Functional Primary Mouse Hepatocytes: Cell Characterization and Asialoglycoprotein Receptor Based Assay Development. *Cytotechnology* **2012**, *64* (2), 187–195.

(69)   Torrance, J. D.; Bothwell, T. H. A Simple Technique for Measuring Storage Iron Concentrations in Formalinised Liver Samples. *S Afr J Med Sci.* **1968**, *33* (1), 9–11.

Supporting Information

Results and Discussion

Polymer Synthesis and Characterization
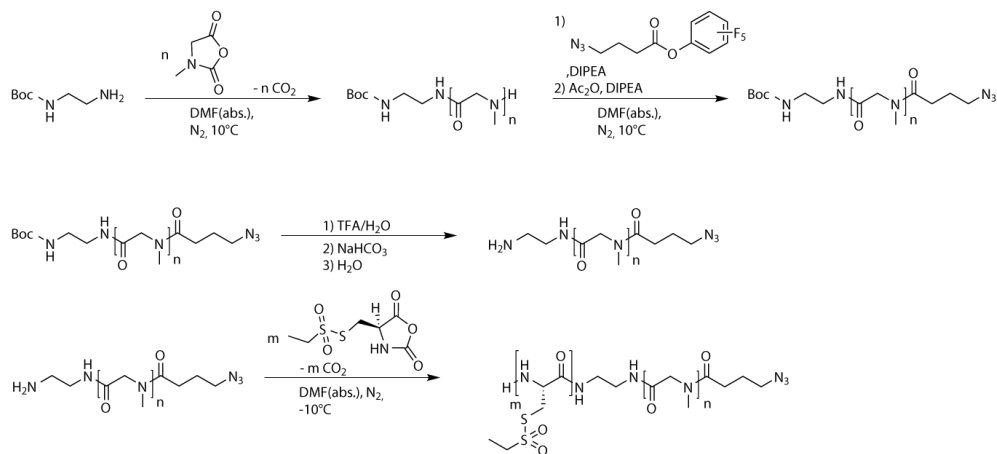
Scheme S1. Polymerization scheme for azide-functionalized pSar$_n$-*block*-pCys(SO$_2$Et)$_m$ (**P1** to **P3**) copolypepti(o)ides.

Table S1. Characterization of pSar$_n$-*block*-pCys(SO$_2$Et)$_m$ (**P1** to **P3**) copolymers.

polymer	end-group	X_n (pSar)[a]	X_n (pCys(SO$_2$Et))[b]	wt.% Cys(SO$_2$Et)	M_n[c] / kDa	$Đ$[b]
P1	Ac	225	31	27.5	31.2	2.64
P2	N$_3$	200	17	18.9	31.7	1.25
P3	N$_3$	170	27	30.4	35.1	7.06

[a] HFIP-GPC, relative to pSar standards. [b] as determined by ^{1}H-NMR. [c] HFIP-GPC, relative to PMMA standards.
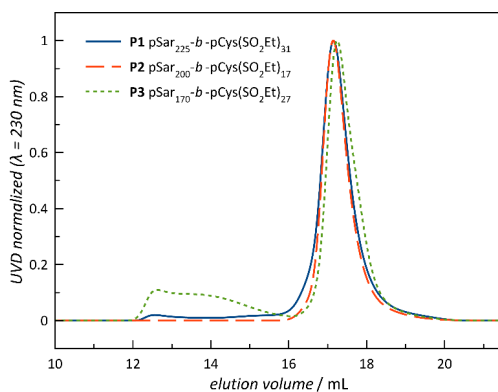
Figure S1. HFIP-GPC traces of **P1-P3** (see Table 1). Note that secondary structures are not suppressed in the eluent (HFIP containing 3 g·L⁻¹ of CF₃COOK), and elution volumes may be influenced by the degree of secondary structure formation of the pCys(SO₂Et)$_m$ block, as reported by previously.[1-3]
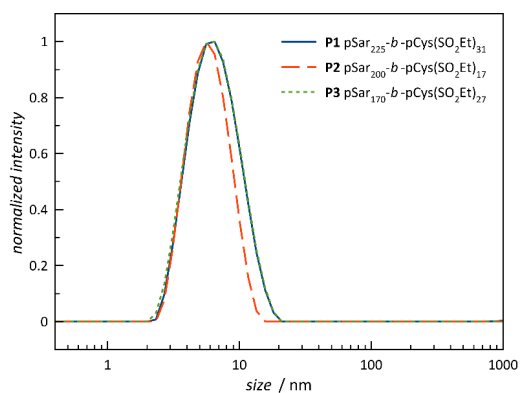
Figure S2. Single-angle DLS of pSar-b-pCys(SO₂Et) block copolymers (**P1** - **P3**) in DMSO (ß = 18 g·L⁻¹) confirms the absence of larger structures but polymer species only.
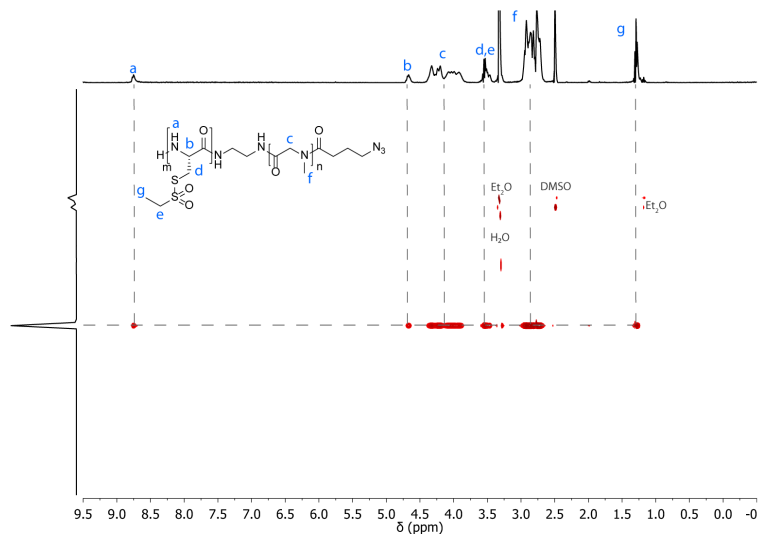
Figure S3. ^{1}H DOSY NMR spectrum of **P1** (pSar$_{225}$-*block*-pCys(SO$_2$Et)$_{31}$) in DMSO-d_6.
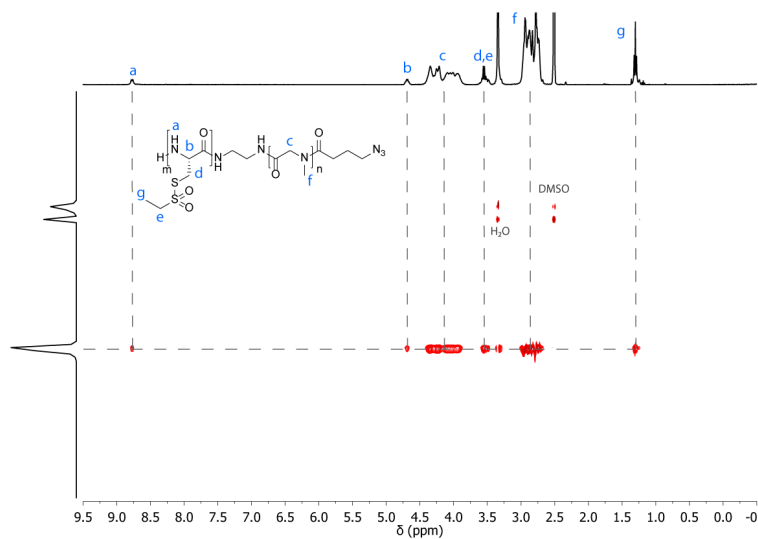
Figure S4. ^{1}H DOSY NMR spectrum of **P2** (pSar$_{200}$-*block*-pCys(SO$_2$Et)$_{17}$) in DMSO-d_6.
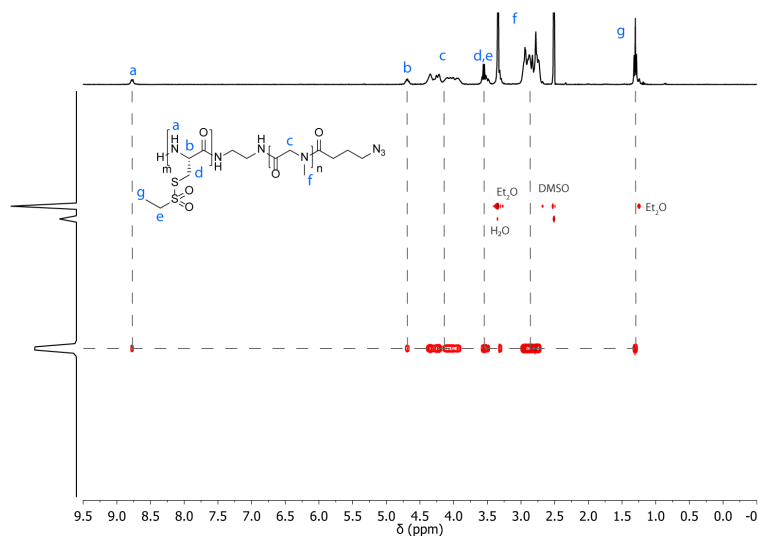
Figure S5. ^{1}H DOSY NMR spectrum of **P3** (pSar$_{170}$-*block*-pCys(SO$_2$Et)$_{27}$) in DMSO-d_6.

Nanoparticle Characterization

Table S2. Characterization of core cross-linked polymeric micelles with and without embedded iron oxide nanoparticles.

particle	polymer	cross-linker	yield	D_h / nm[a]	PDI[a]	$wt.\%$ Fe_2O_3[b]	N_{Dye}[c]
SPION-CCPM^{Cy5}	P3	Lipoic acid	22%	82	0.163	33	16.5
SPION-CCPM^{Cy5}#2	P2	Lipoic acid	36%	63	0.122	42	4.1
CCPMs^{Cy5}	P1	*N*-3-Azidopropyl-liponamide	46%	49	0.131	-	2.5

[a] determined by single-angle DLS. [b] determined by TGA in O$_2$ atmosphere. [c] determined by FCS.
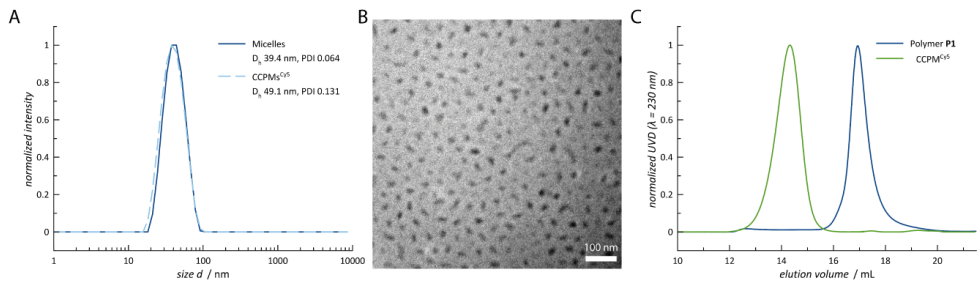
Figure S6. Characterization of CCPM control particles. (**A**) DLS analysis shows core cross-linked polymeric micelles (CCPMS) with narrow dispersity. (**B**) CryoTEM confirmed the presence of nanoparticles with sizes well below 100 nm with spherical morphology. (**C**) HFIP GPC analysis confirmed successful cross-linking.
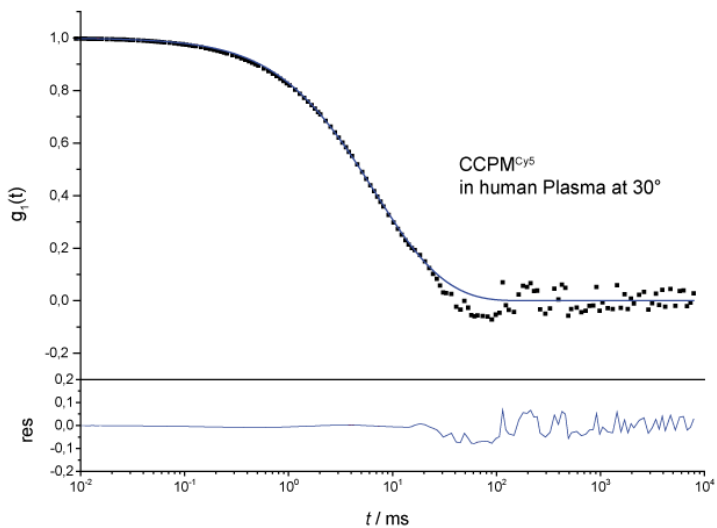
Figure S7. Multi-angle DLS shows no aggregation or increasing sizes for CCPM[Cy5] after incubation in human plasma.
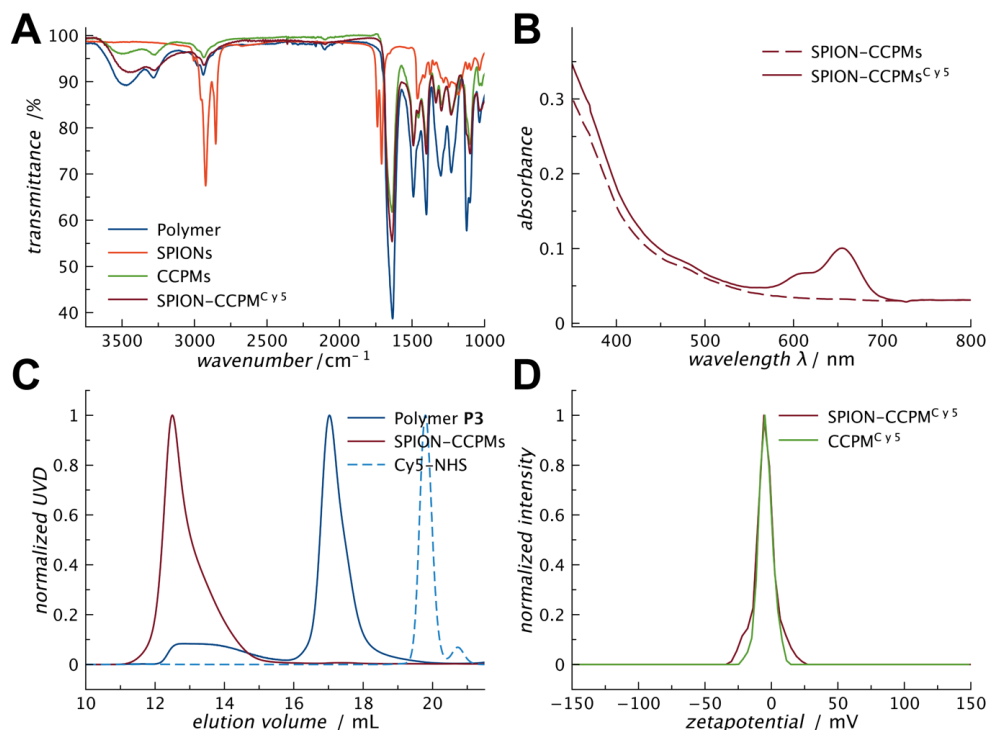
Figure S8. Characterization of SPION-CCPMs (**A**) ATR-FT-IR Spectroscopy of SPION-CCPMs, CCPMs, SPIONs and block copolymer pSar-*b*-pCys(SO$_2$Et). (**B**) UV-Vis spectroscopy of SPION-CCPM dispersions in water. Strong absorbance below $\lambda = 500$ nm refers to embedded iron oxide nanoparticles. Distinct absorbance of Cy5 can be detected for SPION-CCPM[Cy5] after dye conjugation and purification. (**C**) GPC-analysis in HFIP implies stable cross-linking and absence of residual unconjugated dye or polymer for SPION-CCPM[Cy5]. The multimodal GPC-trace for polymer P3 is attributed to ß-sheet induced aggregation (see Figure S1). (**D**) Zeta potential distribution. Slightly negative zeta-potentials were determined for both, SPION-CCPM[Cy5] and CCPM[Cy5], in 3 mM sodium chloride solution.
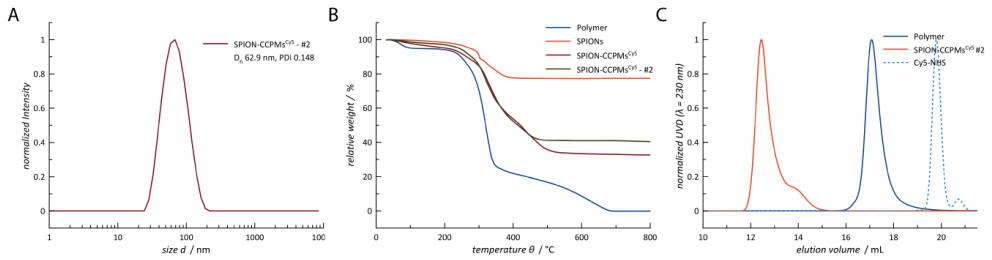
Figure S9. Characterization of SPION-CCPM^{Cy5} #2 particles. (**A**) DLS analysis reveals SPION-CCPM^{Cy5} #2 particles with narrow dispersity. (**B**) TGA analysis confirms higher iron oxide contents for SPION-CCPM^{Cy5} #2 (42 wt.%) compared to SPION-CCPM^{Cy5} (33 wt.%). (**C**) HFIP GPC analysis confirmed successful cross-linking and removal of unconjugated dye or polymer.
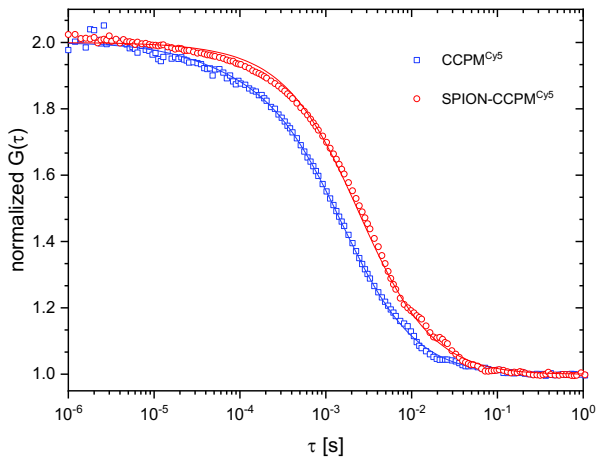
Figure S10. Fluorescence correlation spectroscopy. Normalized autocorrelation curves of Cy5-labelled SPION-CCPMs^{Cy5} (red circles) and CCPMs^{Cy5} (blue squares) measured in PBS buffer. The solid lines represent the corresponding fits with eq. 2 (main text). The fitting was done using single component ($m = 1$ in eq. 2) that confirms the absence of unconjugated dye.
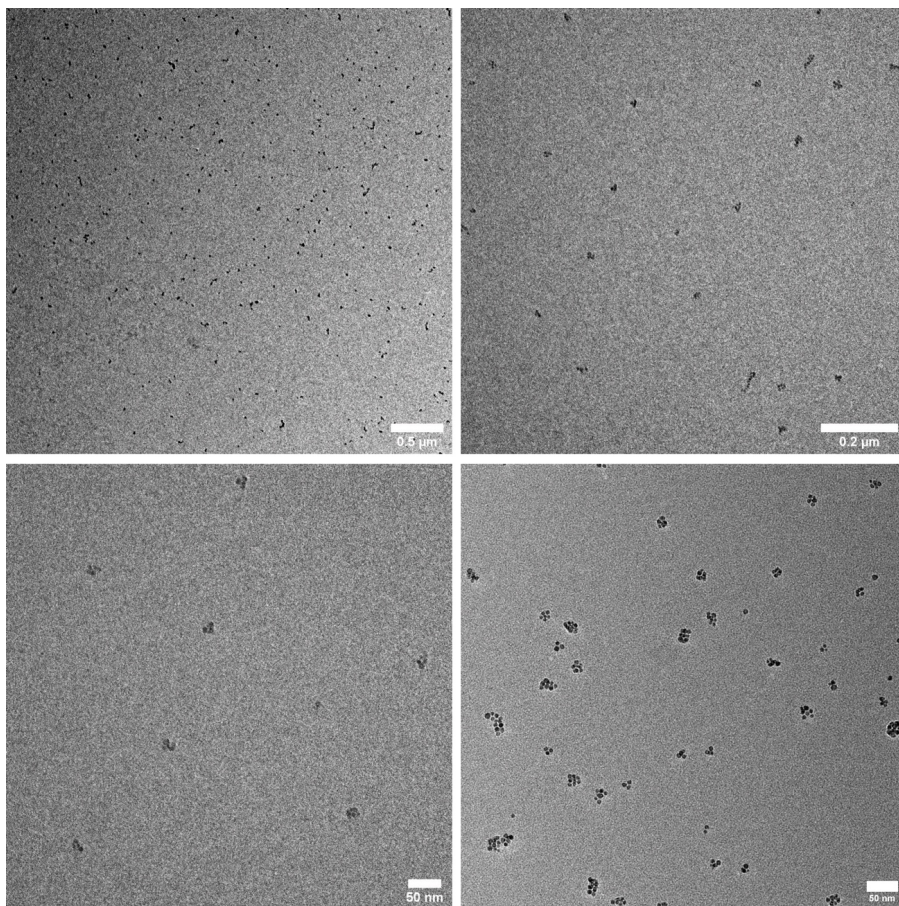
Figure S11. Additional TEM images of SPION-CCPMs^{Cy5}.
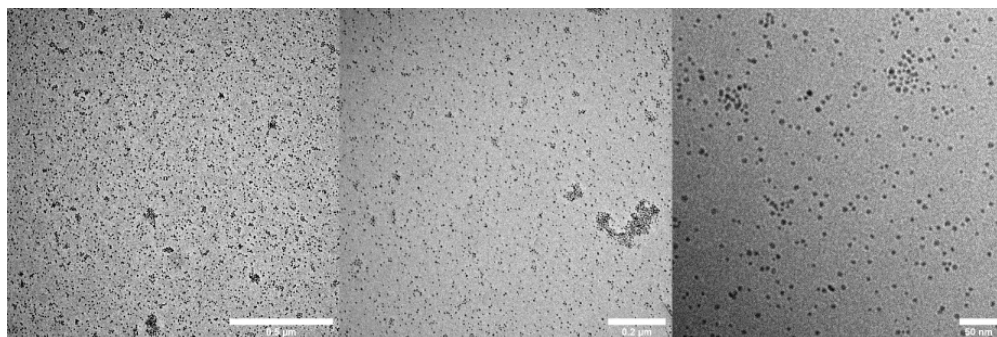
Figure S12. TEM images of oleic acid coated SPIONs. No organized clusters of nanoparticles can be detected.

Magnetic Response & Guidance

A

B
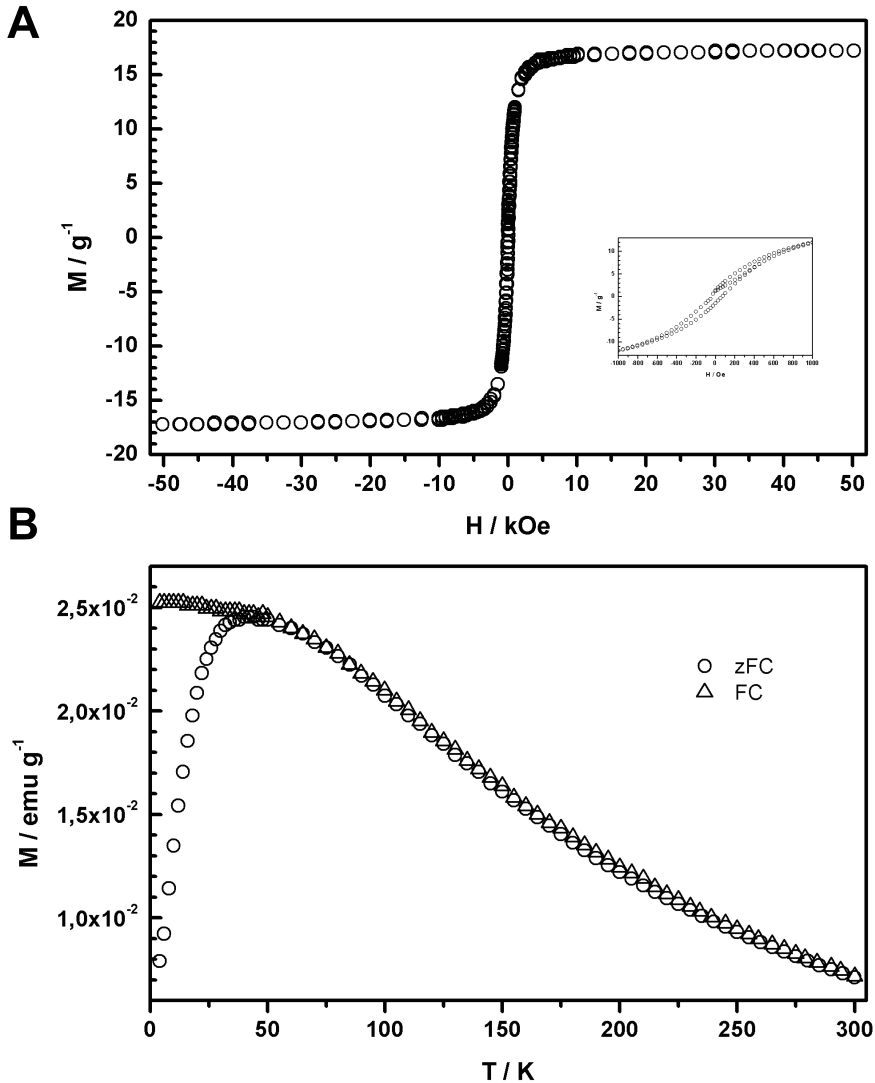
Figure S13. (**A**) Magnetization hysteresis loop recorded for SPION-CCPMs at 5 K conforms superparamagnetic behavior. (**B**) Zero field cooling/field cooling curves revealed a blocking temperature of 42 K, confirming the presence of superparamagnetic iron oxide nanoparticles.[4]
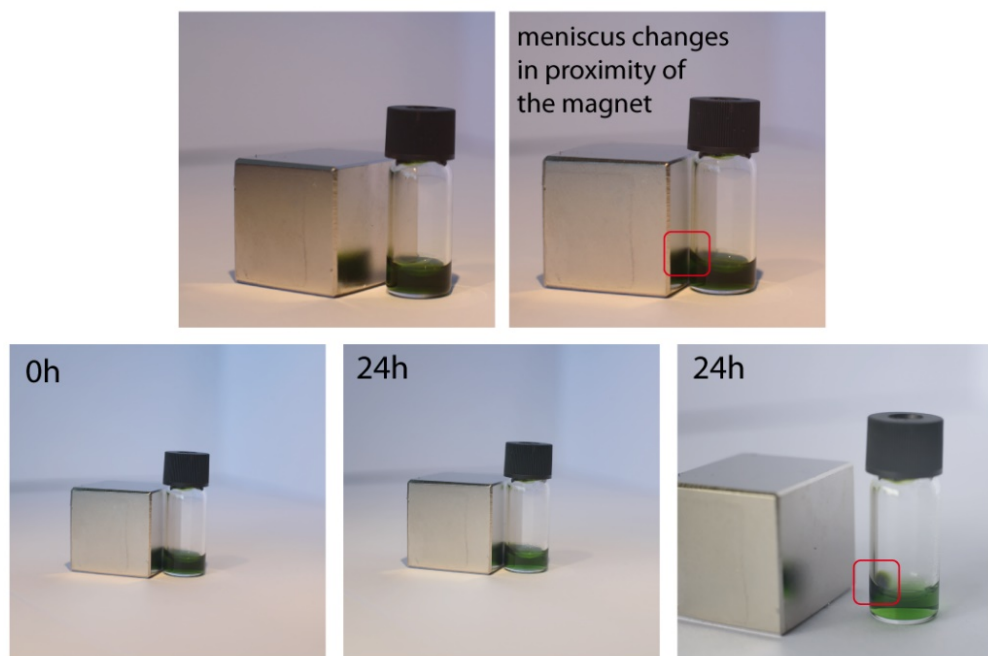
Figure S14. Images of the magnetic response of SPION-CCPM^Cy5 dispersions in water. (upper images) In proximity of a permanent magnet, the meniscus of the dispersion changes immediately. (lower images) Slow accumulation of SPION-CCPM^Cy5 by magnetic force.
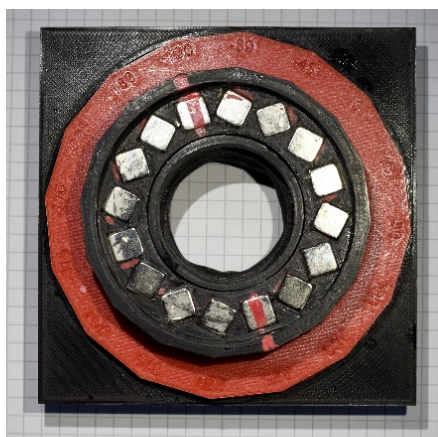
Figure S15. Image of the quadrupolar/dipolar ring-type magnet used for magnetic guidance experiments.[5]

Magnetic Guidance in vivo

If a magnetic particle should be moved against a blood stream, the magnetic force, F_{mag}, must overcome the hydrodynamic (Stokes) friction, F_{fric}. A straight-forward calculation then gives

$$F_{mag} > F_{\text{fric}} \tag{S1}$$

$$mG = \varrho VMG > 6\pi\eta R_h v \tag{S2}$$

Where m [Am²] is the magnetic moment of the particle and G [T·m⁻¹] the magnetic field gradient. It is more useful to express m by a magnetization per mass M [Am²·kg⁻¹] times its mass or density (ρ [kg·m⁻³]) times particle volume (V [m³]). On the other side of the equation, the dynamic viscosity, η [Pa·s], of the surrounding liquid, its velocity, v [m·s⁻¹], relative to a sphere with hydrodynamic radius, R_h [m], is determining the friction. If, like in our case, a larger particle contains N spherical SPION centers of radius R, this can be rearranged to find the necessary field gradient to counter the blood flow:

$$G > \frac{9 \cdot v \cdot \eta \cdot R_h}{2 \cdot \rho \cdot N \cdot R^3 \cdot M} \tag{S3}$$

Equation S3. Approximation of the magnetic gradient required to direct magnetic particles in dispersion of a fluid in motion.

with v as the velocity of the blood flow ($2 \cdot 10^{-3}$ m·s⁻¹ (zebrafish embryo)[6], 0.15 m·s⁻¹ (human)[7]), η as the dynamic viscosity of the blood ($5 \cdot 10^{-3}$ Pa·s (zebrafish embryo)[6], $3.5 \cdot 10^{-3}$ Pa·s (human)[8]), R_h as the hydrodynamic radius of the SPION-CCPM nanoparticle, ρ as the density of the nanoparticle (approx. 1500 kg·m⁻³ for SPION-CCPMs), R as the radius magnetic SPION core, and M as the saturation magnetization of the SPION nanoparticle (50 Am²·kg⁻¹ for 10 nm iron oxide nanoparticles, 74 Am²·kg⁻¹ for magnetite nanoparticles > 20 nm).[4]

For SPION-CCPMs with R_h = 40 nm, each containing 5 SPIONs cores of R = 5 nm, the magnetic gradient needs to be larger than $3.84 \cdot 10^7$ T·m⁻¹ or $2.02 \cdot 10^9$ T·m⁻¹ to overcome the velocity of the blood flow and guide those nanoparticles in the vasculature of zebrafish embryos or humans. For SPION-CCPMs with increased dimension of the magnetic cores (R_h = 20 nm, R_{SPION} = 10 nm, N = 3) values slightly decrease to $2.70 \cdot 10^6$ T·m⁻¹ or $1.42 \cdot 10^8$ T·m⁻¹ for zebrafish embryos or humans, still by far extending the capabilities of the displayed magnet guidance system (G = 2.5 T·m⁻¹).[5]
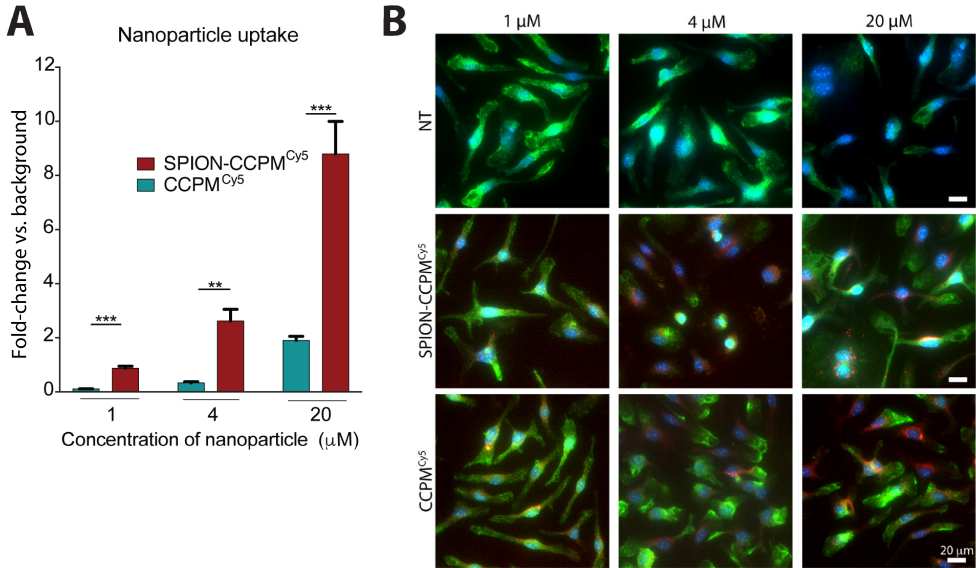
Macrophage Uptake & Stimulation

Figure S16. Concentration dependent uptake of SPION-CCPMs[Cy5] and CCPMs[Cy5] in BMDMs. (**A** and **B**) Non-treated (NT) BMDMs, or BMDMs treated with increasing concentrations of SPION-CCPMs[Cy5] or CCPMs[Cy5] (red) for 24 hrs. (**A**) Internalization of nanoparticles was measured by FACS fluorescence detection (intensity of Cy5). (**B**) Representative images of BMDMs with and without nanoparticle treatment. Cells were stained with Iba1 (green), a cell surface marker for macrophages, and DAPI. Data reported as mean ± SEM, n = 3 independent experiments. One-way ANOVA (black): * $p < 0.01$, ** $p < 0.001$, *** $p < 0.0001$.
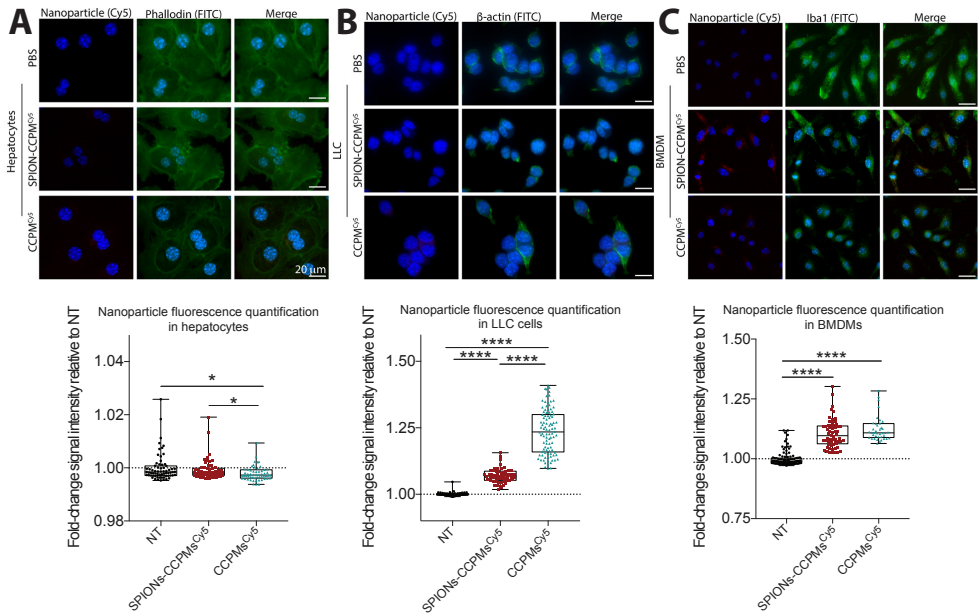
Figure S17. Uptake of SPION-CCPMs and CCPMs in primary murine Hepatocytes, LLCs and BMDMs. Cells were incubated with SPION-CCPMs or CCPMs. Amount of SPION-CCPMs added to cells was calculated based on iron concentration from the core and the amount of CCPMs was calculated to match the mass of CCPMs contained within SPION-CCPMs. (**A**) Representative images of primary hepatocytes, (**B**) Lewis Lung Cancer Cells (LLCs), and (**C**) BMDMs treated with SPION-CCPMsCy5 or CCPMsCy5 (red) for 24 hours. Quantification of nanoparticle signal within cells is below each respective cell type, whereby at least n = 30 cells was analyzed. Primary hepatocytes and LLCs were stained with Phallodin or β-actin (green) and DAPI (blue). BMDMs were stained with Iba1 antibody (green). Data reported as n ± Standard Error of the Mean (SEM). One-way ANOVA: * p < 0.01, ** p < 0.001, *** p < 0.0001.
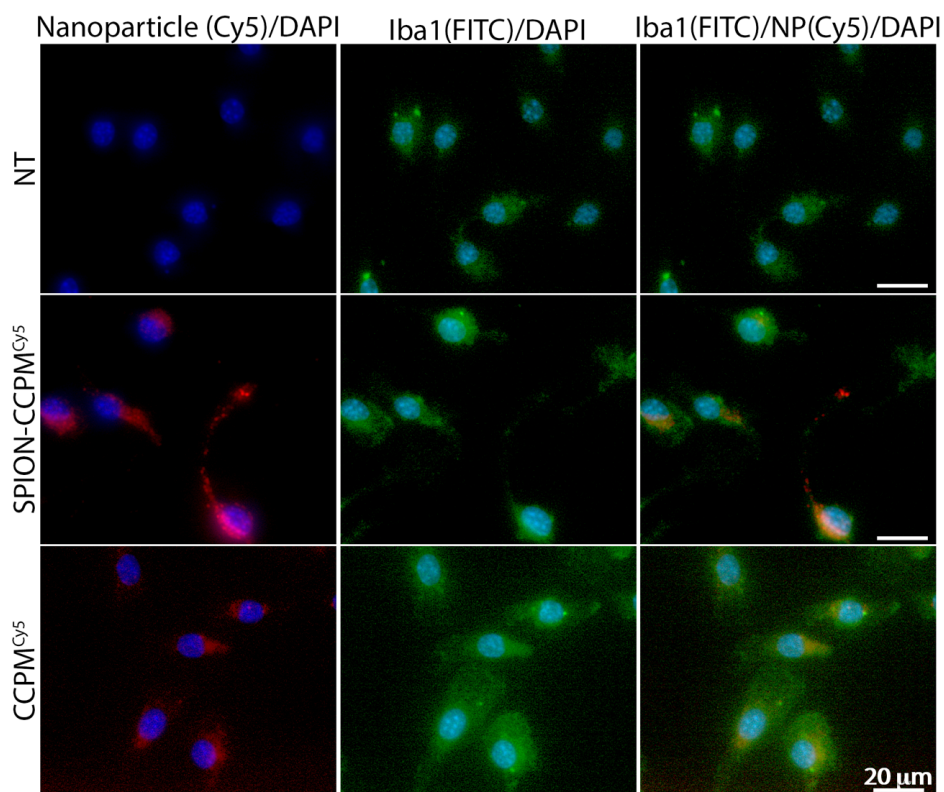
Figure S18. SPION-CCPMs and CCPMs are taken up by BMDMs after a 1-hour incubation. BMDMs were incubated with 20 µM SPION-CCPMs or CCPMs and fixed with 4 % paraformaldehyde after one hour. Cells were stained with a macrophage marker, Iba1 (green), and DAPI (blue).
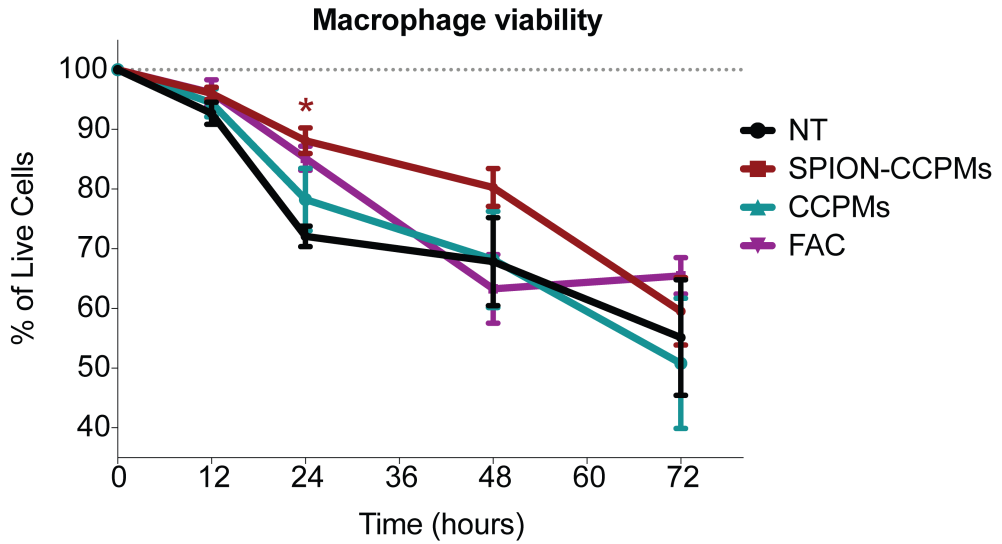
Figure S19. SPION-CCPMs do not cause cytotoxicity in BMDMs. Cells were incubated with 20 mM SPION-CCPMs, dose matched CCPMs, or 20 μM ferric ammonium citrate (FAC). Lactate dehydrogenase (LDH) quantities were measured in the supernatant of cell cultures at 490 nm wavelength after adding CytoTox 96© substrate (Promega). Values are represented as a percentage of the 0 hour condition at each time point. Data reported as n ± SEM. n = 3 independent experiments. One-way ANOVA: * $p < 0.05$, ** $p < 0.01$, *** $p < 0.001$.
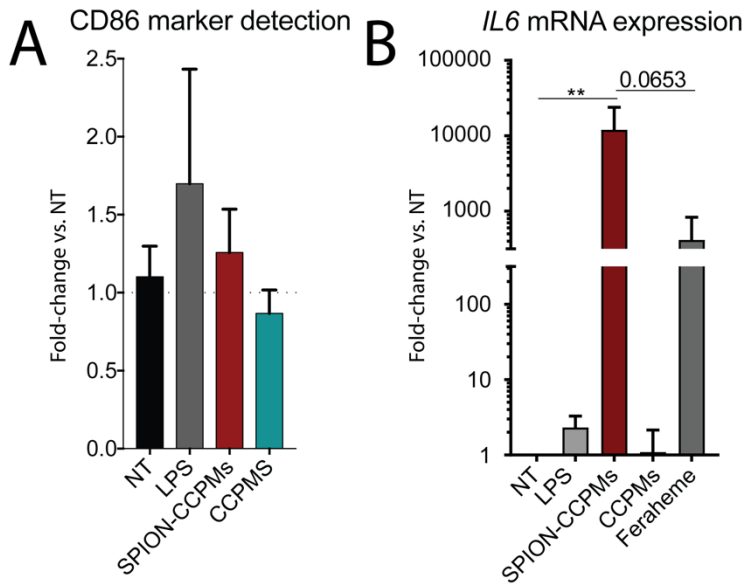
Figure S20. SPION-CCPMs and not CCPMs activate an inflammatory response in human macrophages. (**A** and **B**) Human peripheral monocytes were differentiated for 10 days using M-CSF to produce macrophages. Macrophages were incubated with 20 µM SPION-CCPMs, Feraheme, CCPMs, or 100 ng/mL lipopolysaccharide (LPS). After 24 hours, cells were harvested for FACS analysis to detect the cell surface markers CD80 and CD86 (**A**) or differential cytokine mRNA expression using qPCR (**B**). (**B**) Data show mean and SEM of mRNA expression compared to the non-treated (NT) condition and all samples were corrected for *RPL19* mRNA expression. One-way ANOVA (black): * $p < 0.05$, ** $p < 0.01$, *** $p < 0.001$, **** $p < 0.0001$.
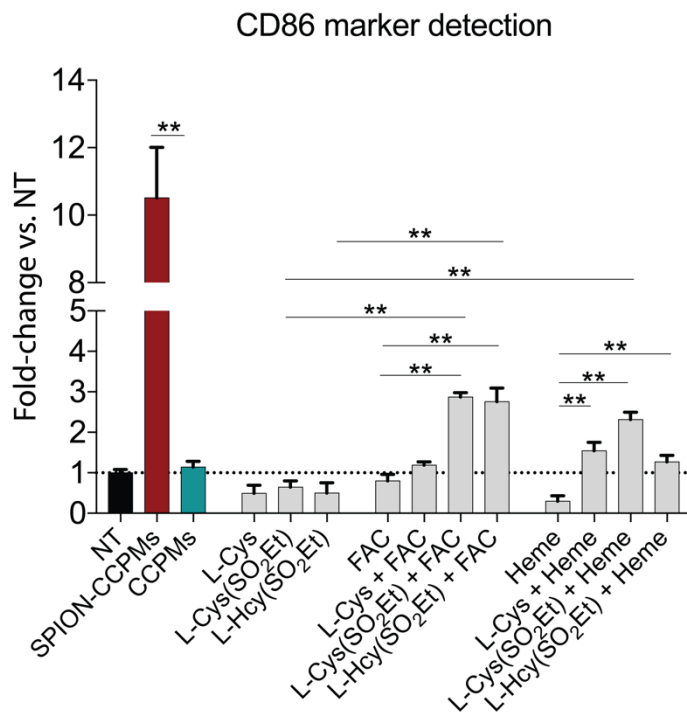
Figure S21. CD86 protein expression in macrophages following treatment with various cysteine dimers. Cells were incubated for 24 hours with 20 µM iron (SPION-CCPMs, heme or ferric ammonium citrate (FAC)), CCPMs, L-cysteine (L-Cys), *S*-ethylsulfonyl-L-cysteine (L-Cys(SO$_2$Et)), *S*-ethylsulfonyl-L-homocysteine (L-Hcy(SO$_2$Et)), and cell surface marker CD86 was measured using fluorescence detection by FACS. Values are represented as fold-change compared to non-treated (NT) condition. Data show mean and SEM, n = 2 independent experiments. One-way ANOVA (black): * $p < 0.05$, ** $p < 0.01$, *** $p < 0.001$, **** $p < 0.0001$.
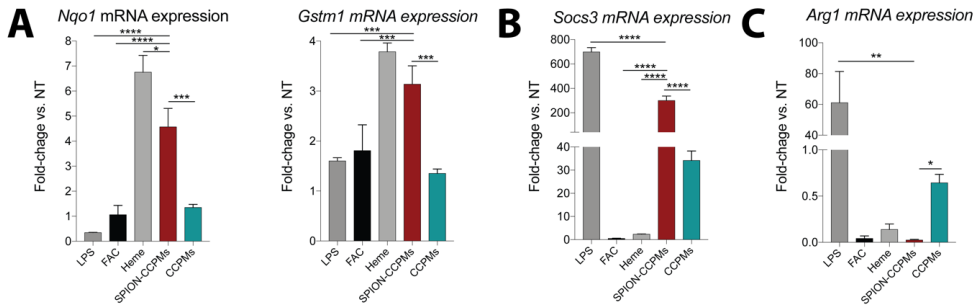
Figure S22. SPION-CCPMs induce sterile inflammation in macrophages. (A-C) BMDMs were incubated with 100 ng/mL LPS, 20 µM FAC, 20 µM Heme, 20 µM SPION-CCPMs or CCPMs for 18 hours. Amount of SPION-CCPMs added to cells was calculated to 20 µM iron from the core and the amount of CCPMs added to cells was calculated to match the mass of CCPMs contained within SPION-CCPMs. The graphs show mean and SEM of mRNA expression compared to the non-treated (NT) condition and all samples were corrected for *Rpl19* mRNA expression. One-way ANOVA (black): * $p < 0.05$, ** $p < 0.01$, *** $p < 0.001$, **** $p < 0.0001$.

Table S3. Antibodies used for Flow Cytometry.

antibody	fluorophore	clone	isotype	manufacturer
Anti-mouse cell culture experimentation				
CD206	Alexa Fluor 700	MR6F3	Rat IgG2b, κ	ThermoFisher
CD38	FITC	90	Rat IgG2a, κ	BioLegend
CD86	Brilliant Violet 421	GL-1	Rat IgG2a, κ	BioLegend
CD80	Brilliant Violet 650	16-10A1	Armenian Hamster IgG	BioLegend
MHC II	PE-Cy7	M5/114.15.2	Rat IgG2b, κ	BioLegend
Anti-mouse *in vivo* experimentation				
CD45	PerCP-Cy5.5	104	N/A	ThermoFisher
Ly6G	FITC	1A8	N/A	BioLegend
Ly6C	PE-Dazzle	HK1.4	N/A	BioLegend
F4/80	BV605	T45-2342	N/A	ThermoFisher
CD11c	PE	N418	N/A	BioLegend
Siglec-F	APC-Cy7	E50-2440	N/A	ThermoFisher
CD11b	PerCP	ICRF44	N/A	ThermoFisher
CD64	BV711	X54-5/7.1	N/A	BioLegend
CD80	BV650	16-10A1	Armenian Hamster IgG	BioLegend
CD71	BV510	RI7217	Rat IgG2a, κ	BioLegend
MerTK	BV421	108928	Rat IgG2a	ThermoFisher
Anti-human				
CD80	PE	2D10	Mouse IgG1, κ	BioLegend
CD86	Alexa Fluor 488	IT2.2	Mouse IgG2b, κ	BioLegend

Table S4. Primers for quantitative RT-PCR (*mus musculus*).

| gene	sequence
Arg1	Forward 5' AATCTGCATGGGCAACCTGT 3' Reverse 5' GTCTACGTCTCGCAAGCCAA 3'
Cxcl10	Forward 5' ACGTGTTGAGATCATTGCCAC 3' Reverse 5' GTCGCACCTCCACATAGCTT 3'
Fpn1	Forward 5' TGTCAGCCTGCTGTTTGCAGGA 3' Reverse 5' TCTTGCAGCAACTGTGTCACCG 3'
Gstm1	Forward 5' TCCGTGCAGACATTGTGGAG 3' Reverse 5' CTGCTTCTCAAAGTCAGGGTTG 3'
Ho-1	Forward 5' AGGCTAAGACCGCCTTCCT 3' Reverse 5' TGTGTTCCTCTGTCAGCATCA 3'
Il6	Forward 5' GCTACCAAACTGGATATAATCAGGA 3' Reverse 5' CCAGGTAGCTATGGTACTCCAGAA 3'
Il1β	Forward 5' GCAACTGTTCCTGAACTCAACT 3' Reverse 5' ATCTTTTGGGGTCCGTCAACT 3'
Nos2	Forward 5' TGGAGACTGTCCCAGCAATG 3' Reverse 5' CAAGGCCAAACACAGCATACC 3'
Nqo1	Forward 5' AGCGTTCGGTATTACGATCC 3' Reverse 5' AGTACAATCAGGGCTCTTCTCG 3'
Rpl19	Forward 5' AGGCATATGGGCATAGGGAAGAG 3' Reverse 5' TTGACCTTCAGGTACAGGCTGTG 3'
Slc7a11	Forward 5' TCCACAAGCACACTCCTCTG 3' Reverse 5' CGTCAGAGGATGCAAAACAA 3'
Socs3	Forward 5' CCTTTGACAAGCGGACTCTC 3' Reverse 5' GCCAGCATAAAAACCCTTCA 3'
Tfr1	Forward 5' CCCATGACGTTGAATTGAACCT 3' Reverse 5' GTAGTCTCCACGAGCGGAATA 3'
Tnfa	Forward 5' TGCCTATGTCTCAGCCTCTTC 3' Reverse 5' GAGGCCATTTGGGAACTTCT 3'

Table S5. Primers for quantitative RT-PCR (*homo sapiens*).

gene	sequence
IL6	Forward 5' AAATTCGGTACATCCTCGACGGA 3'
	Reverse 5' GGAAGGTTCAGGTTGTTTTCTGC 3'
IL1β	Forward 5' CTCGCCAGTGAAATGATGGCT 3'
	Reverse 5' GTCGGAGATTCGTAGCTGGAT 3'
RPL19	Forward 5' TCGCCTCTAGTGTGTCCTCCG 3'
	Reverse 5' GCGGCCCAAGGTGTTTTTC 3'
TNFα	Forward 5' ATGAGCACTGAAAGCATGATCC 3'
	Reverse 5' GAGGGCTGATTAGAGAGAGGTC 3'

References for Supporting Information

(1)   Schäfer, O.; Huesmann, D.; Barz, M. Poly(S -Ethylsulfonyl- l -Cysteines) for Chemoselective Disulfide Formation. *Macromolecules* **2016**, *49* (21), 8146–8153.

(2)   Huesmann, D.; Birke, A.; Klinker, K.; Türk, S.; Räder, H. J.; Barz, M. Revisiting Secondary Structures in NCA Polymerization: Influences on the Analysis of Protected Polylysines. *Macromolecules* **2014**, *47* (3), 928–936.

(3)   Bauer, T. A.; Muhl, C.; Schollmeyer, D.; Barz, M. Racemic S -(Ethylsulfonyl)- Dl -cysteine N -Carboxyanhydrides Improve Chain Lengths and Monomer Conversion for B-Sheet-Controlled Ring-Opening Polymerization. *Macromol. Rapid Commun.* **2021**, *42* (8), 2000470.

(4)   Demortière, A.; Panissod, P.; Pichon, B. P.; Pourroy, G.; Guillon, D.; Donnio, B.; Bégin-Colin, S. Size-Dependent Properties of Magnetic Iron Oxidenanocrystals. *Nanoscale* **2011**, *3* (1), 225–232.

(5)   Baun, O.; Blümler, P. Permanent Magnet System to Guide Superparamagnetic Particles. *J. Magn. Magn. Mater.* **2017**, *439*, 294–304.

(6)   Chen, C. Y.; Patrick, M. J.; Corti, P.; Kowalski, W.; Roman, B. L.; Pekkan, K. Analysis of Early Embryonic Great-Vessel Microcirculation in Zebrafish Using High-Speed Confocal MPIV. *Biorheology* **2011**, *48* (5–6), 305–321.

(7)   Schmidt, R. F.; Lang, F.; Heckmann, M. *Physiologie Des Menschen*; **2010**.

(8)   Brandes, R.; Busse, R. *Kreislauf. Physiologie des Menschen*; **2010**; p 576f.

Appendix

^{1}H NMR Spectra
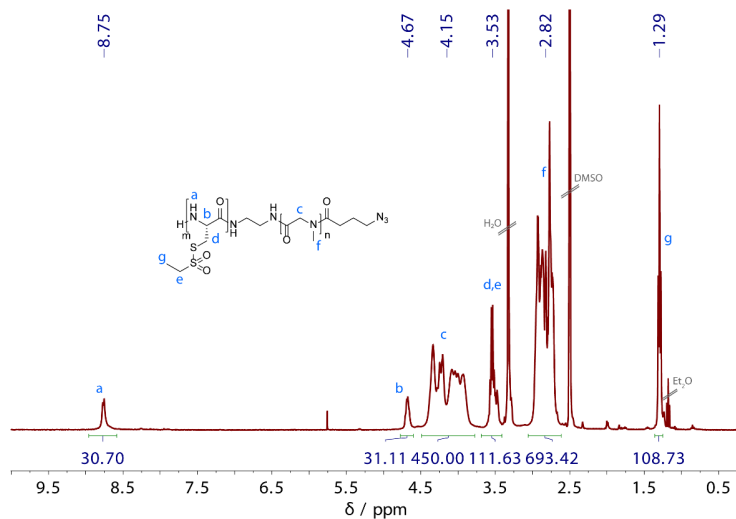
Figure S23. ^{1}H NMR spectrum of **P1** (pSar$_{225}$-*block*-pCys(SO$_2$Et)$_{31}$) in DMSO-d_6.
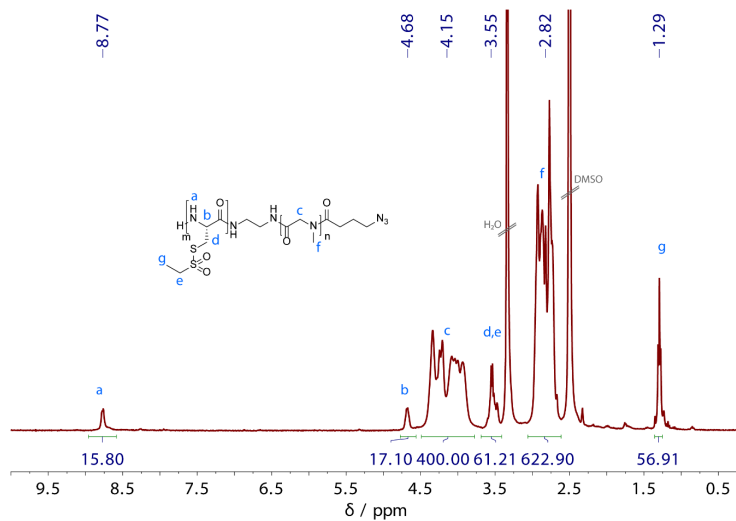
Figure S24. ^{1}H NMR spectrum of **P2** (pSar$_{200}$-*block*-pCys(SO$_2$Et)$_{17}$) in DMSO-d_6.
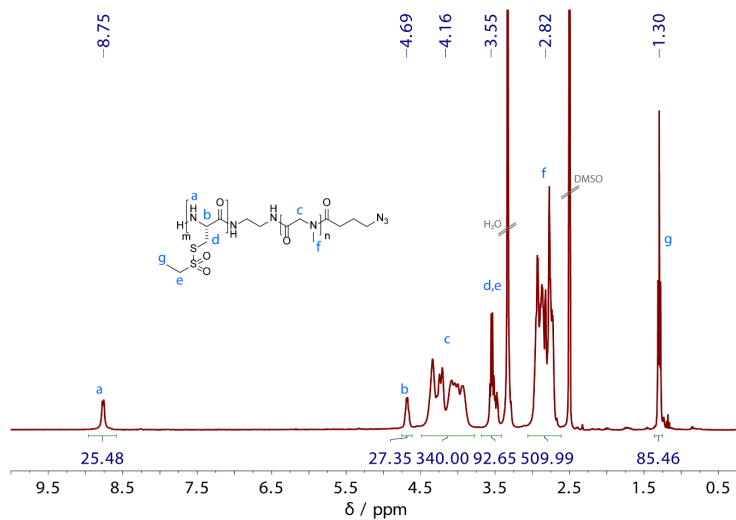
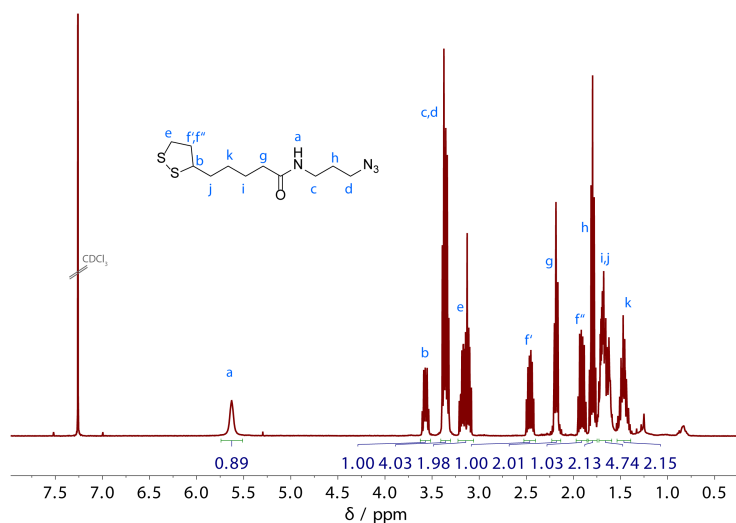**Figure S25.** ^{1}H NMR spectrum of **P3** (pSar$_{170}$-*block*-pCys(SO$_2$Et)$_{27}$) in DMSO-d_6.

Figure S26. ^{1}H NMR spectrum *N*-3-azidopropyl liponamide in CDCl$_3$.